RESEARCH ARTICLE

WILEY

# Two-level Fourier analysis of multigrid for higher-order finite-element discretizations of the Laplacian

## Yunhui He | Scott MacLachlan

Department of Mathematics and
Statistics, Memorial University of
Newfoundland, St. John's, Canada

**Correspondence**
Yunhui He, Department of Mathematics
and Statistics, Memorial University of
Newfoundland, St. John's NL A1C 5S7,
Canada.
Email: yunhui.he@mun.ca

**Summary**
In this paper, we employ local Fourier analysis (LFA) to analyze the convergence properties of multigrid methods for higher-order finite-element approximations to the Laplacian problem. We find that the classical LFA smoothing factor, where the coarse-grid correction is assumed to be an ideal operator that annihilates the low-frequency error components and leaves the high-frequency components unchanged, fails to accurately predict the observed multigrid performance and, consequently, cannot be a reliable analysis tool to give good performance estimates of the two-grid convergence factor. While two-grid LFA still offers a reliable prediction, it leads to more complex symbols that are cumbersome to use to optimize parameters of the relaxation scheme, as is often needed for complex problems. For the purposes of this analytical optimization as well as to have simple predictive analysis, we propose a modification that is "between" two-grid LFA and smoothing analysis, which yields reasonable predictions to help choose correct damping parameters for relaxation. This exploration may help us better understand multigrid performance for higher-order finite element discretizations, including for $Q_2$-$Q_1$ (Taylor-Hood) elements for the Stokes equations. Finally, we present two-grid and multigrid experiments, where the corrected parameter choice is shown to yield significant improvements in the resulting two-grid and multigrid convergence factors.

**KEYWORDS**
finite-element method, higher-order elements, Jacobi iteration, local Fourier analysis, multigrid

## 1 | INTRODUCTION

Multigrid methods[1–5] are very popular to solve the linear systems that arise from the discretization of many partial differential equations (PDEs). The choice of the multigrid components, such as grid transfer operators and the relaxation scheme, has a great influence on the performance of these algorithms. In this paper, we focus on the Poisson problem,

$$\begin{cases} -\Delta u(x) = f(x), & x \in \Omega, \\ u(x) = g(x), & x \in \partial\Omega, \end{cases} \tag{1}$$

discretized using higher-order finite elements. In the literature, there are many efficient multigrid methods for problem (1), see works of Heys et al.[6] and Trottenberg et al.[7] It is worthwhile, however, to understand how these methods work

efficiently. Local Fourier analysis (LFA)[5,7] has proven a good tool for theoretical investigation and multigrid method design, including for the curl–curl equation,[8,9] parabolic partial differential equations,[10,11] the Stokes equations,[9,12,13] poroelasticity equations,[14] and the Poisson equation.[7,15,16]

LFA provides two common approaches to estimate the convergence factor of a two-grid method, known as the LFA smoothing factor and the two-grid LFA convergence factor. The simpler LFA smoothing factor is an appealing tool to optimize algorithmic parameters of the relaxation scheme, but is known to not always be predictive of true performance. In contrast, two-grid LFA couples different harmonic frequencies, leading to more complicated formulations where similar theoretical analysis is much more challenging. Under the assumption that we have an "ideal" coarse-grid-correction operator that annihilates low-frequency error components and leaves high-frequency components unchanged, then LFA smoothing analysis and two-grid LFA both give good predictions for the actual multigrid performance. However, some recent studies have reported that the LFA smoothing factor fails to accurately predict some multigrid results (e.g., Friedhoff and MacLachlan[10,17]). Since the LFA smoothing factor does not offer its usual predictivity of multigrid convergence behavior for the space-time diffusion equation and its generalizations, Friedhoff and MacLachlan[17] develop new tools to make up for the failure of standard smoothing analysis to provide insight into the asymptotic convergence behavior of multigrid methods for these problems. MacLachlan and Oosterlee[9] present an LFA for general problems, focusing on analyzing the complementarity between relaxation and coarse-grid correction (CGC) within multigrid solvers for systems of PDEs with finite-element discretizations. In that paper, the smoothing factor of LFA overestimates the two-grid convergence factor for the Taylor-Hood ($Q_2$-$Q_1$) discretization of the Stokes equations. However, no further explanation is given. We aim to design a simpler analysis (in comparison to two-grid LFA) to offer reliable predictions.

To our knowledge, the vast majority of existing LFA for the Poisson problem focuses on discretization using finite differences or linear finite elements.[3,5,7] In contrast, Hemker et al.[15] study the convergence of a multigrid method for the solution of a linear second-order elliptic equation by discontinuous Galerkin methods. The cell-centered finite-difference discretization on triangular grids is considered by Rodrigo et al.[16] A variant of LFA is applied to discretization matrices arising from Galerkin B-spline isogeometric analysis in the work of Donatelli et al.,[18] focusing on two-level analysis in place of classical smoothing analysis. Similar work, by de la Riva et al.[19] shows some agreement between the LFA smoothing and two-grid factors for isogeometric analysis with overlapping Schwarz relaxation. Recently, Rodrigo et al.[20] proposed a generalized *multicolor* LFA to study the convergence of multigrid for quadratic finite element discretizations, with corresponding definitions of multicolor LFA smoothing factors and two-grid convergence factors. They analyze several relaxation schemes with this approach, again finding often poor agreement between the multicolor smoothing and two-grid convergence factors.

Here, we focus on standard higher-order finite-element discretizations of Poisson's equation with weighted Jacobi relaxation, and use LFA to understand performance. In contrast to the cases of standard finite-difference or (bi)linear finite-element discretizations, we will see that the LFA smoothing factor does not offer a good prediction of performance in the higher-order case. We focus on weighted Jacobi relaxation as a representative of the Jacobi–Chebyshev relaxation often considered for $Q_2$ (and other) discretizations; see, for example, the work of May et al.[21]

In the literature, there are many studies about higher-order methods for different types of PDEs. The spectral element method for second-order problems was studied both numerically and theoretically in the works of Maday et al.[22] and Rønquist et al.,[23] showing good smoothing properties of simple Jacobi relaxation for the Laplace problem. The impact of different higher-order finite-element discretizations for the Laplace problem on multigrid convergence, with Richardson and Jacobi relaxation, was considered by Köster et al.[24] Comparison of different multigrid methods for higher-order finite-element discretizations, either as stationary iterations or as preconditioners, was reported in the work of Sundar et al.[25] There, the convergence behavior was seen to strongly depend on the polynomial order when multigrid is used as a preconditioner, but not for multigrid as a standalone iteration. Other studies of higher-order finite-element methods and multigrid include those for nonlinear problems[26] and the incompressible Navier-Stokes equations.[21,27,28]

Supporting numerical results demonstrate some key conclusions of our analysis. First, there is a notable gap between the classical LFA smoothing factor and the two-grid convergence factor for these elements and these relaxation schemes. The standard LFA assumption of an "ideal" CGC operator, which annihilates the low-frequency error components and leaves the high-frequency components unchanged is not true for higher-order finite-element discretizations, where our results show that the coarse-grid correction process efficiently reduces certain high-frequency errors. Furthermore, minimizing the classical smoothing factor does not minimize the corresponding convergence factor.

The outline of the paper is as follows. In Section 2, we recall the standard definitions of LFA. In Section 3, we analyze the weighted Jacobi relaxation scheme for the $Q_2$ finite-element approximation in one dimension (1D) and show how to obtain optimal parameters to minimize the convergence factor. We extend this analysis to higher-order finite-elements in Section 4. In Section 5, two-grid LFA is presented for biquadratic Lagrangian elements in two dimensions (2D), and we discuss the optimal parameter choice. Conclusions are presented in Section 6.

## 2 | DEFINITIONS AND NOTATIONS

In order to describe LFA for finite-element methods, we first introduce some terminology for the 1D case; however, it can be easily extended to 2D or three dimensions (3D). More details can be found, for example, in the work of Trottenberg et al.[7] We first consider 1D infinite uniform grids, $G_h$. Let $L_h$ be a scalar Toeplitz operator acting on $l^2(G_h)$

$$L_h \stackrel{\wedge}{=} [s_\kappa]_h \ (\kappa \in V); \ L_h w_h(x) = \sum_{\kappa \in V} s_\kappa w_h(x + \kappa h), \tag{2}$$

with constant coefficients $s_\kappa \in \mathbb{R}$ (or $\mathbb{C}$), where $w_h(x)$ is a function in $l^2(G_h)$. Here, $V$ is taken to be a finite index set of integers, $V \subset \mathbb{Z}$. Note that since $L_h$ is Toeplitz, it is formally diagonalized by the standard Fourier modes, $\psi(\theta, x) = e^{\iota \theta \cdot x/h}$, where $\iota^2 = -1$.

**Definition 1.** We call $\tilde{L}_h(\theta) = \sum_{\kappa \in V} s_\kappa e^{\iota \theta \kappa}$ the symbol of $L_h$.

Note that for all grid functions $\psi(\theta, x)$,

$$L_h \psi(\theta, x) = \tilde{L}_h(\theta) \psi(\theta, x),$$

Here, we consider multigrid methods for finite-element discretizations with standard geometric grid coarsening; that is, we construct a sequence of coarse grids by doubling the mesh size. High and low frequencies for standard coarsening are given by

$$\theta \in T^{\text{low}} = \left[-\frac{\pi}{2}, \frac{\pi}{2}\right), \theta \in T^{\text{high}} = \left[-\frac{\pi}{2}, \frac{3\pi}{2}\right) \setminus \left[-\frac{\pi}{2}, \frac{\pi}{2}\right).$$

The error-propagation operator for a relaxation scheme, represented similarly by a Toeplitz operator $M_h$, applied to a finite-element approximation is

$$S_h(\omega) = I - \omega M_h^{-1} L_h,$$

where $\omega$ is an overall weighting factor.

**Definition 2.** The error-propagation symbol, $\tilde{S}_h(\omega, \theta)$, for relaxation $S_h(\omega)$ on the infinite grid $G_h$ satisfies

$$S_h(\omega)\psi(\theta, x) = \tilde{S}_h(\omega, \theta)\psi(\theta, x), \theta \in \left[-\frac{\pi}{2}, \frac{3\pi}{2}\right),$$

for all $\psi(\theta, x)$, and the corresponding smoothing factor for $S_h(\omega)$ is given by

$$\mu_{\text{loc}} := \mu_{\text{loc}}(S_h(\omega)) = \max_{\theta \in T^{high}} \left\{\left|\tilde{S}_h(\omega, \theta)\right|\right\}. \tag{3}$$

**Definition 3.** Because the smoothing factor is a function of some parameters, let $\mathbf{D}$ be a bounded and closed set of allowable parameters and define the optimal smoothing factor over $\mathbf{D}$ as

$$\mu_{\text{opt}} = \min_{\mathbf{D}} \mu_{\text{loc}}.$$

Definition 1 directly applies to scalar equations with degree of freedoms (DOFs) located on a collocated mesh. However, the $Q_2$ and higher-order finite-element discretizations that we consider here naturally use basis functions associated with different "types" of points on the mesh, leading to stencils that depend on the type of the meshpoint. Such systems cannot be diagonalized by the standard Fourier-mode similarity transformation. However, reordering the DOFs appropriately leads to block-structured matrices with Toeplitz blocks, which can be diagonalized within each block. Thus, we

can treat the discretized system as a linear operator acting on Fourier variables associated with the same frequency but different components of the finite-element space. To our knowledge, this treatment of non-collocated discretizations was first introduced by Boonen et al.,[8] but has been used in several papers since then.[9,29–31]

In what follows, we consider $(q \times q)$ linear systems of operators, which read

$$\mathbf{L}_h = \begin{pmatrix} L_h^{1,1} & \cdots & L_h^{1,q} \\ \vdots & \cdots & \vdots \\ L_h^{q,1} & \cdots & L_h^{q,q} \end{pmatrix}.$$

The $L_h^{i,j}(i,j = 1, 2, \ldots, q)$ are scalar Toeplitz operators. Each entry in $\tilde{\mathbf{L}}_h(\theta)$, the symbol of $\mathbf{L}_h$, is computed as the (scalar) symbol of the corresponding block of $L_h^{i,j}$, following Definition 1. For simplicity, we reuse the notation in Equation (3) for the case of block symbols as described in the following.

On a collocated mesh, all blocks in $\mathbf{L}_h$ are diagonalized by the same transformation. However, in the setting of $Q_2$ elements in 1D, as considered in Section 3, we consider $G_h = G_{h,N} \cup G_{h,C}$, for quadratic Lagrangian elements, with

$$G_{h,N} = \left\{ x_{k,N} := kh, k \in \mathbb{Z} \right\}, \text{ and } G_{h,C} = \left\{ x_{k,C} := kh + h/2, k \in \mathbb{Z} \right\}. \tag{4}$$

Here $G_h$ contains two types of meshpoints, the nodes of the mesh and the cell centers. The coarse grid, $G_{2h}$, is defined similarly. Similar construction is used for higher-order elements in 1D and in 2D, as will be explained later. We note that such a partitioning is necessary for any basis choice for $Q_2$ elements, as the resulting linear system is not Toeplitz, but can be readily permuted into $2 \times 2$ block form with Toeplitz blocks, assuming the same basis is used in each element and that the elements are of uniform size.

Each block $L_h^{i,j}$ in $\mathbf{L}_h$ for $i, j = 1, 2$ is defined as in Equation (2), with $V$ taken to be either a finite index set of integer ($V_N$) or half-integer ($V_C$) values, with $V_N \subset \mathbb{Z}$ and $V_C \subset \left\{ z + \frac{1}{2} | z \in \mathbb{Z} \right\}$. The operators discussed later are naturally treated as block operators, and the Fourier representation of each block can be calculated based on Definition 1, with Fourier bases adapted to account for the staggering of the mesh points. In Definition 2, the symbol $\tilde{S}_h(\omega, \theta)$ will be a matrix, thus, $\left| \tilde{S}_h(\omega, \theta) \right|$ is replaced by $\rho(\tilde{S}_h(\omega, \theta))$, the spectral radius of $\tilde{S}_h(\omega, \theta)$, in Equation (3).

The resulting Fourier functions are $\varphi(\theta, x_k) \in \text{span} \left\{ \varphi_N(\theta, x_k), \varphi_C(\theta, x_k) \right\}$ on $G_h$, in which

$$\varphi_N(\theta, x_k) = \left( e^{i\theta \cdot x_{k,N}/h} \ 0 \right)^T, \varphi_C(\theta, x_k) = \left( 0 \ e^{i\theta \cdot x_{k,C}/h} \right)^T,$$

where $T$ denotes the (non-conjugate) transpose of the row vectors. Because $\varphi(\theta, x_k)$ is periodic in $\theta$ with period $2\pi$, we consider the domain $\theta \in \left[ -\frac{\pi}{2}, \frac{3\pi}{2} \right)$.

The LFA smoothing factor plays a very important role in LFA. In many cases, LFA smoothing analysis gives good predictions for the actual multigrid performance, under the assumption that we have an "ideal" coarse-grid-correction operator that annihilates low-frequency error components and leaves high-frequency components unchanged. However, in our setting, this assumption about ideal CGC will be seen to not hold (due to the discretization), but the two-grid LFA convergence factor still offers useful predictions. We next give a brief introduction to two-grid LFA.

**Definition 4.** The $2h$-harmonics, $\mathcal{F}_{2h}(\theta)$, which will be used for the two-grid analysis, are given by

$$\mathcal{F}_{2h}(\theta) = \text{span} \left\{ \varphi_h(\theta^0, x), \varphi_h(\theta^1, x) \right\},$$

with $\theta = \theta^0 \in T^{\text{low}} := \Theta_{2h}$, and $\theta^\alpha = \theta + \alpha\pi$, where $\alpha = 0, 1$.

Assume a two-grid operator with $\nu_1$ pre- and $\nu_2$ postrelaxation steps is defined as,

$$\mathcal{M}_h^{\text{TGM}}(\omega) = S_h^{\nu_2}(\omega)\mathcal{M}_h^{\text{CGC}}S_h^{\nu_1}(\omega), \tag{5}$$

where

$$\mathcal{M}_h^{\text{CGC}} = I - PA_{2h}^{-1}RA_h,$$

where $R$ and $P$ are the restriction and interpolation operators, respectively, and $A_{2h}$ is the natural rediscretized operator on the coarse grid, but can also be the Galerkin operator (or any other choice).

Inserting Fourier representations of $S_h, A_h, A_{2h}, R$, and $P$ into Equation (5), we obtain the Fourier representation of the two-grid error-propagation operator as

$$\hat{\mathcal{M}}_h^{\text{TGM}}(\omega, \theta) = \hat{S}_h^{\nu_2}(\omega, \theta) \left( I - \hat{P}(\theta)(\tilde{A}_{2h}(2\theta))^{-1} \hat{R}(\theta) \hat{A}_h(\theta) \right) \hat{S}_h^{\nu_1}(\omega, \theta), \tag{6}$$

where

$$\hat{A}_h(\theta) = \text{diag} \left\{ \tilde{A}_h(\theta), \tilde{A}_h(\theta + \pi) \right\}, \quad \hat{S}_h(\omega, \theta) = \text{diag} \left\{ \tilde{S}_h(\omega, \theta), \tilde{S}_h(\omega, \theta + \pi) \right\},$$
$$\hat{P}(\theta) = \left( \tilde{P}(\theta); \tilde{P}(\theta + \pi) \right), \quad \hat{R}(\theta) = \left( \tilde{R}(\theta), \tilde{R}(\theta + \pi) \right),$$

in which diag$\{A, B\}$ stands for the block diagonal matrix with diagonal blocks $A$ and $B$.

The asymptotic two-grid convergence factor, $\rho_{\text{asp}}$, is defined as

$$\rho_{\text{asp}} = \sup \left\{ \rho(\hat{\mathcal{M}}_h^{\text{TGM}}(\omega, \theta)) : \theta \in \Theta_{2h} \right\}. \tag{7}$$

In what follows, we consider a discrete form of $\rho_{\text{asp}}$, denoted by $\rho$, resulting from sampling $\rho_{\text{asp}}$ over only a finite set of frequencies spaced at intervals of $\frac{\pi}{64}$. No substantial change was observed in the reported results when finer spacing was used. Since $\rho(AB) = \rho(BA)$ and we primarily consider two-grid cycles, we consider only the case of prerelaxation; that is $\nu_2 = 0$. Unless otherwise stated, we focus on the case of a single relaxation step per multigrid cycle, with $\nu_1 = 1$.

# 3 | LFA FOR QUADRATICS IN 1D

Here, we consider the discretization of problem (1) in 1D, using quadratic ($Q_2$) finite elements, and nodal basis functions defined at the nodes of the mesh and cell centers (but the analysis could be modified for other bases), and will focus on weighted Jacobi relaxation.

## 3.1 | Quadratic Lagrangian elements

For these quadratic Lagrangian elements, the elementary contributions to the stiffness and mass matrices as $3 \times 3$ symmetric matrices are

$$\text{EK}_h = \frac{1}{3h} \begin{pmatrix} 7 & -8 & 1 \\ -8 & 16 & -8 \\ 1 & -8 & 7 \end{pmatrix}, \quad \text{EM}_h = \frac{h}{30} \begin{pmatrix} 4 & 2 & -1 \\ 2 & 16 & 2 \\ -1 & 2 & 4 \end{pmatrix},$$

respectively. We can decompose the resulting stencils into connections among and between the DOFs located at the nodes of the mesh and those located at cell centers. The node-to-node connections yield the stencils

$$\frac{1}{3h} \begin{bmatrix} 1 & 14 & 1 \end{bmatrix} \quad \text{and} \quad \frac{h}{30} \begin{bmatrix} -1 & 8 & -1 \end{bmatrix}.$$

The node-to-center stencils are given by

$$\frac{1}{3h} \begin{bmatrix} -8 & \star & -8 \end{bmatrix} \quad \text{and} \quad \frac{h}{30} \begin{bmatrix} 2 & \star & 2 \end{bmatrix},$$

with transposed connections between centers and nodes, where $\star$ stands for the DOF position in the off-diagonal blocks. The center-to-center stencils are diagonal,

$$\frac{1}{3h} \begin{bmatrix} 16 \end{bmatrix} \quad \text{and} \quad \frac{h}{30} \begin{bmatrix} 16 \end{bmatrix}.$$

On the infinite grid $G_h$, each of these stencils defines a Toeplitz operator on $l^2(G_{h,*})$ and, so, the block systems can be block diagonalized by considering the invariant subspace given by linear combinations of $\varphi_N(\theta, x)$ and $\varphi_C(\theta, x)$. The resulting block symbols of the stiffness and mass operators are

$$\tilde{A}_h(\theta) = \frac{1}{3h} \begin{pmatrix} 14 + 2\cos\theta & -16\cos\frac{\theta}{2} \\ -16\cos\frac{\theta}{2} & 16 \end{pmatrix}, \quad \tilde{B}_h(\theta) = \frac{h}{30} \begin{pmatrix} 8 - 2\cos\theta & 4\cos\frac{\theta}{2} \\ 4\cos\frac{\theta}{2} & 16 \end{pmatrix}, \tag{8}$$

respectively. The error-propagation symbol of weighted Jacobi relaxation is given by

$$\tilde{S}_h(\omega, \theta) = I - \omega\tilde{M}_h^{-1}(\theta)\tilde{A}_h(\theta), \tag{9}$$

where $\tilde{M}_h(\theta)$ is the symbol of the diagonal operator,

$$M_h = \frac{1}{3h} \begin{pmatrix} 14I & 0 \\ 0 & 16I \end{pmatrix}. \tag{10}$$

This follows from the node-to-node and center-to-center stencils given above, noting that the diagonal part of the matrix $A_h$ is $M_h$.

Using Equations (8) and (10), we plot the distribution of eigenvalues of $\tilde{M}_h^{-1}(\theta)\tilde{A}_h(\theta)$, at the left of Figure 1. Note that as a block symbol, $\tilde{M}_h^{-1}(\theta)\tilde{A}_h(\theta)$ has two eigenvalues, each of which can be seen to be a continuous function of $\theta/\pi$. To derive an analytical expression for the eigenvalues of $\tilde{M}_h^{-1}(\theta)\tilde{A}_h(\theta)$, we note that the determinant of $\tilde{M}_h^{-1}(\theta)\tilde{A}_h(\theta) - \lambda I$ is

$$(\lambda - 1)(\lambda - 1 - \frac{\cos\theta}{7}) - \frac{4}{7}(1 + \cos\theta).$$

Let $\lambda_+$ and $\lambda_-$ be the eigenvalues of $\tilde{M}_h^{-1}(\theta)\tilde{A}_h(\theta)$; from above, we have

$$\lambda_\pm = \frac{14 + \cos\theta \pm \sqrt{\cos^2(\theta) + 112\cos\theta + 112}}{14}.$$

Taking $x = \cos\theta$, then we can write

$$\lambda_+(x) = \frac{14 + x + \sqrt{x^2 + 112x + 112}}{14}, \quad \lambda_-(x) = \frac{14 + x - \sqrt{x^2 + 112x + 112}}{14}.$$

It is easy to check that

$$\lambda_+(x)_{\max} = \lambda_+(1) = \frac{15}{7}, \quad \lambda_+(x)_{\min} = \lambda_+(-1) = 1,$$

$$\lambda_-(x)_{\max} = \lambda_+(-1) = \frac{6}{7}, \quad \lambda_-(x)_{\min} = \lambda_-(1) = 0.$$

We plot $\lambda_+(x)$, $\lambda_-(x)$ at the right of Figure 1.

Throughout this paper, we denote $\lambda_{\max,H}$ and $\lambda_{\min,H}$ as the biggest and smallest eigenvalues over only the high frequency range, respectively. Since $\lambda_-(x) < \lambda_+(x)$, for high frequencies ($x \in [-1, 0]$), we have

$$\lambda_{\max,H} = \lambda_+(0) = \frac{7 + 2\sqrt{7}}{7}, \quad \lambda_{\min,H} = \lambda_-(0) = \frac{7 - 2\sqrt{7}}{7}.$$
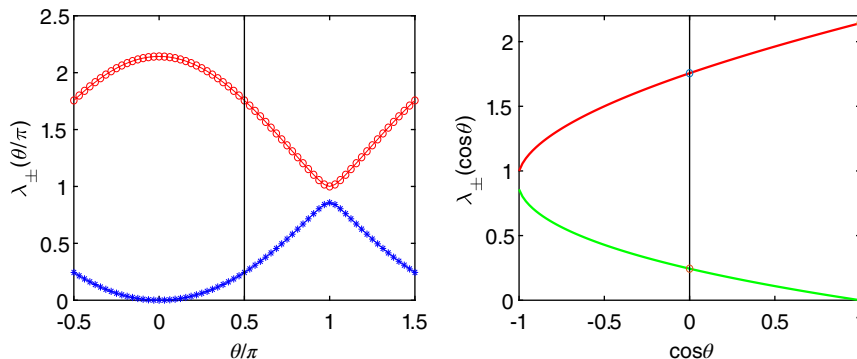


**FIGURE 1** At left, the distribution of the two eigenvalues of $\tilde{M}_h^{-1}(\theta)\tilde{A}_h(\theta)$ as a function of $\theta/\pi$. At right, the distribution of the two eigenvalues of $\tilde{M}_h^{-1}(\theta)\tilde{A}_h(\theta)$, as a function of $\cos\theta$

Thus, the classical optimal choice of $\omega$ that minimizes the resulting smoothing factor for relaxation scheme (9) is given by

$$\omega^* = \frac{2}{\lambda_{\min,H} + \lambda_{\max,H}} = 1, \tag{11}$$

and the corresponding smoothing factor is

$$\mu_2^* = \min_{\omega} \max_{\theta \in T^{\text{high}}} \left| \lambda(\tilde{S}_h(\omega, \theta)) \right| = \frac{2\sqrt{7}}{7} \approx 0.756.$$

Note, however, that this choice of $\omega^*$ leads to a diverging relaxation scheme, as $|1 - \omega^* \lambda_+(1)| > 1$. While this might be acceptable assuming ideal CGC, it is worrisome from the perspective of robustness of the resulting multilevel algorithm. Thus, we consider another relaxation weight,

$$\omega^{**} = \frac{2}{\lambda_{\max}^* + \lambda_{\min,H}} = \frac{14}{22 - 2\sqrt{7}} \approx 0.838, \tag{12}$$

where $\lambda_{\max}^*$ is the biggest of all eigenvalues; that is $\lambda_{\max}^* = \lambda_+(1) = \frac{15}{7}$. For this choice, the corresponding smoothing factor is

$$\mu_2^{**} = \max_{\theta \in T^{\text{high}}} \left| \lambda(\tilde{S}_h(\omega^{**}, \theta)) \right| = \frac{4 + \sqrt{7}}{11 - \sqrt{7}} \approx 0.795.$$

To understand and compare these choices, we now consider two-grid LFA and measured two-grid performance. We use the notation $TG(\nu)$ and $V(\nu)$ to indicate the cycle type and the number of prerelaxation steps employed, that is, $\nu_1 = \nu$ and $\nu_2 = 0$ in the notation of Equation (5). While there is no difference in performance between use of pre- and postrelaxation in the two-grid case, differences can arise in the case of $V$ cycles. We observe, however, that the convergence rates when using pre- or postrelaxation within $V$ cycles are almost equal in the case considered here. We consider the homogeneous problem, $A_h x_h = b = 0$, with discrete solution $x_h \equiv 0$, and start with a random initial guess, $x_h^{(0)}$, to test the multigrid convergence factor. For multigrid cycles, the coarsest grid is a mesh with four elements in 1D, and $4 \times 4$ elements in 2D. Rediscretization is used to define the coarse-grid operator, and we consider only the case of Dirichlet boundary conditions. Here, we use the defects $d_h^{(k)} (k = 1, 2, \cdots$, with $d_h^{(k)} = b - A_h x_h^{(k)})$ to experimentally measure the convergence factor as $\hat{\rho}_h = \frac{\|d_h^{(k)}\|_2}{\|d_h^{(k-1)}\|_2}$ (see Trottenberg et al.[7]). To minimize numerical error in estimating these factors, we report the per-cycle convergence factor measured in the iteration, $k$, at which the $\ell_2$ norm of the residual achieves a factor of $10^{-100}$ times its original value in the case of a converging iteration, or $10^{100}$ times its original value in the case of a diverging iteration. All two-grid and multigrid results were obtained using firedrake[32,33] for the finite-element discretization, and portable, extensible toolkit for scientific computation (PETSc)[34,35] for the multigrid implementation. For comparison, we present the LFA-predicted convergence factors, $\rho$, for two-grid cycles with $\nu$ prerelaxation steps (see Equation (7)).

In Table 1, we first use $\omega^*$ from Equation (11) as the weight. Note that the LFA convergence factor is larger than the smoothing factor. As noted earlier, while we see convergence for $\nu_1 + \nu_2 < 3$, we see divergence when $\nu_1 + \nu_2 = 3$ or 4 for the two-grid method. Furthermore, even though the smoothing factor fails to predict the convergence factor, we see that the measured convergence factor matches well with the LFA-predicted two-grid convergence factor. For $\omega = \omega^{**}$, Table 1 shows a good improvement in the convergence factor compared with the choice of $\omega^*$. We again see a good agreement

**TABLE 1** Two-grid convergence factors for the $Q_2$ approximation in one dimension with Jacobi weights $\omega^*$ and $\omega^{**}$

| | $\omega = \omega^* = 1.000, \mu^* = 0.756$ | | | | $\omega = \omega^{**} = \frac{14}{22-2\sqrt{7}} \approx 0.838, \mu^{**} = 0.796$ | | | |
| --- | --- | --- | --- | --- | --- | --- | --- | --- |
| | $TG(1)$ | $TG(2)$ | $TG(3)$ | $TG(4)$ | $TG(1)$ | $TG(2)$ | $TG(3)$ | $TG(4)$ |
| $\rho$ | 0.821 | 0.985 | 1.118 | 1.279 | 0.526 | 0.495 | 0.372 | 0.302 |
| $\hat{\rho}_{h=1/128}$ | 0.821 | 0.985 | 1.119 | 1.279 | 0.526 | 0.494 | 0.370 | 0.300 |
| $\hat{\rho}_{h=1/256}$ | 0.821 | 0.985 | 1.119 | 1.279 | 0.526 | 0.494 | 0.371 | 0.301 |

between the measured convergence factor and the LFA-predicted two-grid convergence factor, but now the two-grid convergence factor is smaller than the smoothing factor, in contrast to the case of $\omega^*$. Moreover, while the smoothing factor for the choice of $\omega^{**}$ is larger than that of $\omega^*$, the two-grid factor is much better.

## 3.2 | Two-grid LFA in 1D

Two natural questions are raised by these results. First, why is the LFA smoothing factor such a bad predictor of performance? Secondly, is $\omega^{**}$ the best choice for a weight, in terms of two-grid performance? To answer these questions, we consider two-grid LFA in more detail.

The symbols $\tilde{A}_h(\theta)$ and $\tilde{A}_h(\theta + \pi)$ are given in Section 3.1, while the symbols for relaxation are

$$\tilde{S}_h(\omega, \theta) = I - \omega \tilde{M}_h^{-1}(\theta)\tilde{A}_h(\theta), \ \tilde{S}_h(\omega, \theta + \pi) = I - \omega \tilde{M}_h^{-1}(\theta + \pi)\tilde{A}_h(\theta + \pi),$$

and

$$\tilde{A}_{2h}(2\theta) = \frac{1}{6h} \begin{pmatrix} 14 + 2\cos(2\theta) & -16\cos\theta \\ -16\cos\theta & 16 \end{pmatrix}.$$

We note that, as is usual in LFA, the restriction operator maps a function in the harmonic space $\mathcal{F}_{2h}(\theta)$ onto a single Fourier frequency, $2\theta$, on the coarse grid, while interpolation maps from this frequency back to $\mathcal{F}_{2h}(\theta)$. To derive symbols for the grid-transfer operators, we first consider an arbitrary restriction operator characterized by a constant coefficient stencil $R \overset{\wedge}{=} [r_\kappa]$. Then, an infinite grid function $w_h : G_h \to \mathbb{R}$ (or $\mathbb{C}$) is transferred to the coarse grid, $G_{2h}$, in the following way:

$$(Rw_h)(x) = \sum_{\kappa \in V} r_\kappa w_h(x + \kappa h) \ (x \in G_{2h}). \tag{13}$$

When considering discretizations on staggered meshes, when different "types" of variables interact in the interpolation and restriction operators, LFA of these operators cannot be done as in the scalar case. MacLachlan and Oosterlee[9] discussed Fourier representations of grid-transfer operators for general staggered meshes in the context of systems of PDEs, but their results can also be applied to scalar operators discretized on staggered meshes. In the $Q_2$ case, we have two types of grid points on the fine and coarse grids, and the restriction operator can be decomposed based on the partitioning of DOFs associated with the nodes of the mesh and the cell centers on the coarse grid. Finally, the grid transfer operators are treated as block operators. That is, $R$ in Equation (13) will be split into different blocks corresponding to the DOFs on coarse-grid $G_{2h}$, with a similar structure for interpolation. In the following, we show how to define the symbol of a restriction operator for each block in $R := [R_N, R_C]$ (as described below), defined on a staggered mesh.

Let $\varphi_h(\theta^\alpha, x) = e^{i\theta^\alpha x/h}$. We have the following equality

$$\varphi_h(\theta^\alpha, x) = e^{i\alpha\pi x/h}\varphi_{2h}(2\theta^0, x), \quad \text{for all } x \in G_{2h}. \tag{14}$$

Note that $\varphi_h(\theta^\alpha, x)$ coincides on $G_{2h,N}$ with the respective grid function $\varphi_{2h}(2\theta^0, x)$, since $e^{i\alpha\pi x/h} \equiv 1$ in Equation (14), when $x = 2jh$ for $j \in \mathbb{Z}$. However, $e^{i\alpha\pi x/h} = (-1)^\alpha$ when $x = 2(j + \frac{1}{2})h$ coincides with a point in $G_{2h,C}$.

Based on the above discussion, if $R$ only acts on $x \in G_{2h,N}$, we have

$$(R\varphi_h)(\theta^\alpha, \cdot)(x) = \sum_{\kappa \in V} r_\kappa e^{i(x+\kappa h)\theta^\alpha/h} = \sum_{\kappa \in V} r_\kappa e^{i\kappa\theta^\alpha} e^{ix\alpha\pi/h} e^{i2x\theta^0/(2h)} = \sum_{\kappa \in V} r_\kappa e^{i\kappa\theta^\alpha} \varphi_{2h}(2\theta^0, x). \tag{15}$$

In contrast, if $R$ only acts on $x \in G_{2h,C}$, we have

$$(R\varphi_h)(\theta^\alpha, \cdot)(x) = \sum_{\kappa \in V} r_\kappa e^{i\kappa\theta^\alpha}(-1)^\alpha \varphi_{2h}(2\theta^0, x). \tag{16}$$

Note that we can rewrite Equations (15) and (16) in a unified form, given by

$$(R\varphi_h)(\theta^\alpha, \cdot)(x) = \sum_{\kappa \in V} r_\kappa e^{i\kappa\theta^\alpha} e^{i\alpha\pi x/h} \varphi_{2h}(2\theta^0, x).$$

Then, we can naturally define a general form of Fourier representation of a restriction operator.

**Definition 5.** We call $\tilde{R}(\theta^\alpha) = \sum_{\kappa \in V} r_\kappa e^{\iota \kappa \theta^\alpha} e^{\iota \alpha \pi x/h} := \sum_{\kappa \in V} \tilde{r}_\kappa$ the restriction symbol of $R$.

*Remark* 1. We want to emphasize that when calculating the symbol of a restriction operator that mixes different types of DOFs, we must first split it into the different types of DOFs that it restricts from and to before we can apply Definition 5. If the restriction operator is defined on a collocated mesh, we have only $G_{2h,N}$, and $e^{\iota \alpha \pi x/h} \equiv 1$ in Definition 5, which coincides with the definition of the classical restriction symbol.[5] Under such splittings, the symbols in Definition 5 are independent of $x$. While $e^{\iota \alpha \pi x/h}$ appears in the symbol formulation, it only serves to indicate which type of DOFs $R$ is acting on. For the $Q_2$ case, $x$ is always an even multiple of $h$ for restriction to coarse-grid nodes, giving $e^{\iota \alpha \pi x/h} = 1$ in this case, or $x$ is an odd multiple of $h$ for restriction to centers, and $e^{\iota \alpha \pi x/h} = (-1)^\alpha$ in this case.

In our case, we consider quadratic interpolation, and the corresponding adjoint operator for the restriction of the corrections. In stencil notation, the restriction operators are given by

$$R_N \overset{\wedge}{=} [(r_N)_\kappa] = \begin{bmatrix} 0 & -\frac{1}{8} & 0 & \frac{3}{8} & 1(\star) & \frac{3}{8} & 0 & -\frac{1}{8} & 0 \end{bmatrix}, \tag{17}$$

and

$$R_C \overset{\wedge}{=} [(r_C)_\kappa] = \begin{bmatrix} 0 & \frac{3}{4} & 1(\star) & \frac{3}{4} & 0 \end{bmatrix}, \tag{18}$$

where $N, C$ stand for the node and center points on the coarse grid, respectively, and the $\star$ denotes the position (on the coarse grid) at which the discrete operator is applied. Note that these stencils include contributions from both fine-grid nodes and centers to the coarse-grid quantities. We illustrate these in Figure 2.

As with the fine-grid matrix, both $R_N$ and $R_C$ require values from nodes and centers on the fine grid. We decompose $R_N$ as $[R_N(N), R_N(C)]$ and $R_C$ as $[R_C(N), R_C(C)]$ defined in the following

$$R_N(N) = [1], R_N(C) = [-\frac{1}{8} \quad \frac{3}{8} \quad \star \quad \frac{3}{8} \quad -\frac{1}{8}], \tag{19}$$

$$R_C(N) = [1], R_C(C) = [\frac{3}{4} \quad \star \quad \frac{3}{4}], \tag{20}$$

then apply Definition 5 to each piece separately to obtain the symbol of the restriction operator.

**Theorem 1.** *Define R as in Equations (17) and (18). Then the Fourier representation of R is given by the $(2 \times 4)$-matrix*

$$\hat{R}(\theta) = \begin{pmatrix} \tilde{R}(\theta^0) & \tilde{R}(\theta^1) \end{pmatrix}$$
$$= \begin{pmatrix} 1 & \frac{3\cos(\frac{\theta}{2})-\cos(\frac{3\theta}{2})}{4} & 1 & \frac{-3\sin(\frac{\theta}{2})-\sin(\frac{3\theta}{2})}{4} \\ 1 & \frac{3\cos(\frac{\theta}{2})}{2} & -1 & \frac{3\sin(\frac{\theta}{2})}{2} \end{pmatrix}.$$

*Proof.* Let $x \in G_{2h}$ and consider a fine-grid mode $\varphi(\theta^\alpha, y) = \beta_N \varphi_N(\theta^\alpha, y) + \beta_C \varphi_C(\theta^\alpha, y)$ for $y = x + \kappa h \in G_h$. Clearly the value of $[R\varphi(\theta^\alpha), \cdot](x)$ depends on whether $x$ is a node on the coarse grid (and Equation (17) is used) or $x$ is a cell center on the coarse grid (and Equation (18) is used). From Equations (19) and (20), we write the symbol for $R$ in matrix form,

$$\tilde{R}(\theta^\alpha) = \begin{pmatrix} \tilde{R}_N(N, \theta^\alpha) & \tilde{R}_N(C, \theta^\alpha) \\ \tilde{R}_C(N, \theta^\alpha) & \tilde{R}_C(C, \theta^\alpha) \end{pmatrix}, \tag{21}$$
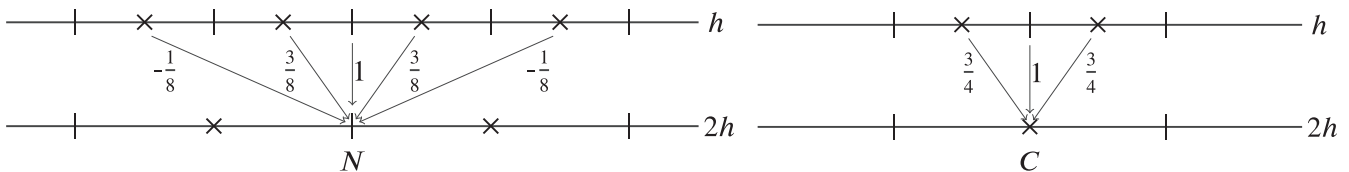


**FIGURE 2** At left, $R_N$-restriction operator. At right, $R_C$-restriction operator

acting on the vector $\left(\beta_N\ \beta_C\right)^T$, where $T$ denotes the (non-conjugate) transpose of the row vectors.

From Equations (19), (20), and Definition 5, we obtain the symbols

$$\tilde{R}_N(N, \theta^\alpha) = 1, \quad \tilde{R}_N(C, \theta^\alpha) = \frac{3}{4}\cos\left(\frac{\theta^\alpha}{2}\right) - \frac{1}{4}\cos\left(\frac{3\theta^\alpha}{2}\right),$$

$$\tilde{R}_C(N, \theta^\alpha) = (-1)^\alpha, \quad \tilde{R}_C(C, \theta^\alpha) = \frac{3}{2}\cos\left(\frac{\theta^\alpha}{2}\right)(-1)^\alpha.$$

Concatenating $\hat{R}(\theta) = \left(\tilde{R}(\theta^0)\ \tilde{R}(\theta^1)\right)$ gives the symbol in the statement of the theorem. ∎

A similar calculation (see the work of MacLachlan and Oosterlee[9]) gives the symbol of quadratic interpolation as

$$\hat{P}(\theta) = \begin{pmatrix} \frac{1}{2} & \frac{1}{2} \\ \frac{3\cos(\frac{\theta}{2})-\cos(\frac{3\theta}{2})}{8} & \frac{3\cos(\frac{\theta}{2})}{4} \\ \frac{1}{2} & -\frac{1}{2} \\ \frac{-3\sin(\frac{\theta}{2})-\sin(\frac{3\theta}{2})}{8} & \frac{3\sin(\frac{\theta}{2})}{4} \end{pmatrix}, \tag{22}$$

satisfying the usual relationship that $\hat{P}(\theta) = \frac{1}{2}(\hat{R}(\theta))^H$, where $H$ denotes the conjugate transpose.

## 3.3 | A lower bound on optimal convergence in 1D

Note that $\rho_{\mathrm{asp}}$ defined in Equation (7) is a function of $\omega$. Our goal is to minimize $\rho_{\mathrm{asp}}$ over all choices of $\omega$, to optimize the resulting multigrid convergence factor. However, this optimization problem involves all $\theta \in \Theta_{2h}$ and is nonconvex and nonsmooth, which poses significant challenges. A natural idea to obtain a lower bound on the best-possible convergence factor is to look at only a single frequency . We now consider the limiting behavior when $\theta \to 0$. When $\theta = 0$, the two eigenvalues of

$$\tilde{S}_h(\omega, \theta + \pi) = I - \omega\tilde{M}_h^{-1}(\theta + \pi)\tilde{A}_h(\theta + \pi),$$

are $1 - \omega$ and $1 - \frac{6}{7}\omega$, and the eigenvector corresponding to $1 - \omega$ is $v_1 = \left(0\ 1\right)^T$.

From Equation (22), when $\theta = 0$, the Fourier representation of the interpolation operator is

$$\hat{P}(0) = \begin{pmatrix} \frac{1}{2} & \frac{1}{2} \\ \frac{1}{4} & \frac{3}{4} \\ \frac{1}{2} & -\frac{1}{2} \\ 0 & 0 \end{pmatrix},$$

and vector $\hat{v}_1 = \left(0\ 0\ 0\ 1\right)^T$ is not in the range of interpolation. Since $\tilde{A}_{2h}(2\theta) = \hat{R}(\theta)\hat{A}_h(\theta)\hat{P}(\theta)$, the symbol of the CGC process acts as the identity on $\mathrm{Range}(\hat{P}(\theta))^\perp$, establishing that $\hat{v}_1$ is an eigenvector of $\hat{\mathcal{M}}_h^{\mathrm{TGM}}(\omega, \theta)$ in the limit as $\theta \to 0$, and allowing us to establish a lower bound on convergence.

**Lemma 1.** *For $\hat{\mathcal{M}}_h^{\mathrm{TGM}}(\omega, \theta)$ defined as in Equation (6),*

$$\mathrm{trace}\left(\lim_{\theta\to 0}\hat{\mathcal{M}}_h^{\mathrm{TGM}}(\omega, \theta)\right) = 2 - \frac{79}{28}\omega.$$

*Proof.* By standard calculation, we have

$$\lim_{\theta\to 0}\hat{\mathcal{M}}_h^{\mathrm{TGM}}(\omega, \theta) = \begin{pmatrix} \frac{7-15\omega}{14} & \frac{-7+15\omega}{14} & \frac{-7+6\omega}{28} & 0 \\ -\frac{7-15\omega}{28} & \frac{-7+15\omega}{28} & -\frac{-7+6\omega}{56} & 0 \\ -\frac{7-15\omega}{14} & -\frac{-7+15\omega}{14} & -\frac{-7+6\omega}{28} & 0 \\ 0 & 0 & 0 & 1-\omega \end{pmatrix}.$$

Thus, trace $\left(\lim_{\theta\to 0}\hat{\mathcal{M}}_h^{\text{TGM}}(\omega,\theta)\right) = \frac{7-15\omega}{14} - \frac{-7+15\omega}{28} - \frac{-7+6\omega}{28} + 1 - \omega = 2 - \frac{79}{28}\omega.$ ∎

Note that $\hat{P}(0)$ is full-rank, so there must be two zero eigenvalues of $\lim_{\theta\to 0}\hat{\mathcal{M}}_h^{\text{TGM}}(\omega,\theta)$. As $1-\omega$ is also an eigenvalue of $\lim_{\theta\to 0}\hat{\mathcal{M}}_h^{\text{TGM}}(\omega,\theta)$, Theorem 1 tells us that the other eigenvalue is $2 - \frac{79}{28}\omega - (1-\omega) = 1 - \frac{51}{28}\omega$. In order to minimize the spectral radius of $\lim_{\theta\to 0}\hat{\mathcal{M}}_h^{\text{TGM}}(\omega,\theta)$, we have the following result.

**Theorem 2.**

$$\min_{\omega}\left\{\max\{|\lambda^*|\} : \lambda^* \in \lambda\left(\lim_{\theta\to 0}\hat{\mathcal{M}}_h^{\text{TGM}}(\omega,\theta)\right)\right\} = \frac{23}{79} \approx 0.291, \tag{23}$$

*and only $\omega = \omega^{***} = \frac{56}{79}$ achieves the minimum.*

*Proof.* Note that the four eigenvalues of $\lim_{\theta\to 0}\hat{\mathcal{M}}_h^{\text{TGM}}(\omega,\theta)$ are 0, 0, $1-\omega$, and $1 - \frac{51}{28}\omega$. Setting $|1-\omega| = |1 - \frac{51}{28}\omega|$, gives $\omega = \frac{56}{79}$. ∎

**Corollary 1.** *For any $\omega$, the optimal two-grid convergence factor for a single relaxation (i.e., $\nu_1 + \nu_2 = 1$) is not less than $\frac{23}{79}$, and this factor can be achieved if and only if $\omega = \omega^{***}$.*

Corollary 1 only tells us that the two-grid convergence factor has a lower bound, but we do not know whether it can be achieved or not. We show this numerically. As above, let $\mu$ and $\rho$ be the LFA-predicted smoothing and two-grid convergence factors, respectively. For $\rho$, we consider only one step of prerelaxation (which gives the same results as one step of postrelaxation). We plot the predicted smoothing and convergence factors as a function of $\omega$ in 1D. The left of Figure 3 indicates that when the classical smoothing factor achieves its optimal value, the corresponding $\omega$ does not minimize the two-grid convergence factor. The choices of $\omega^*$ and $\omega^{**}$ in Equations (11) and (12) both are clearly not the best choice. The left of Figure 3 shows that the optimal $\omega$ is $\omega^{***} = \frac{56}{79} \approx 0.709$, as proposed in Corollary 1. We explore the reasons for this below.

To see that the prediction of Lemma 2 is not a coincidence, we plot the two-grid convergence factor and $\max\left\{|1-\omega|, |1 - \frac{51}{28}\omega|\right\}$ as a function of $\omega$. Comparing the left and right of Figure 3 indicates that, for all $\omega$, the two-grid convergence factor is given by $\max\left\{|1-\omega|, |1 - \frac{51}{28}\omega|\right\}$.

Table 2 confirms that $\omega^{***}$ provides the best observed convergence factor, compared with the choices $\omega^*$ and $\omega^{**}$, shown in Table 1. The two-grid results in Table 2 also confirm that a single sweep of relaxation offers the most cost-effective two-grid cycle. We also present $V$-cycle convergence factors in Table 2, showing similar convergence factors as those of the



**FIGURE 3** At left, local Fourier analysis (LFA)-predicted two-grid convergence and smoothing factors as a function of $\omega$. At right, LFA-predicted two-grid convergence factor and $\max\{|\lambda^*|\}$ as a function of $\omega$ for the $Q_2$ approximation in one dimension
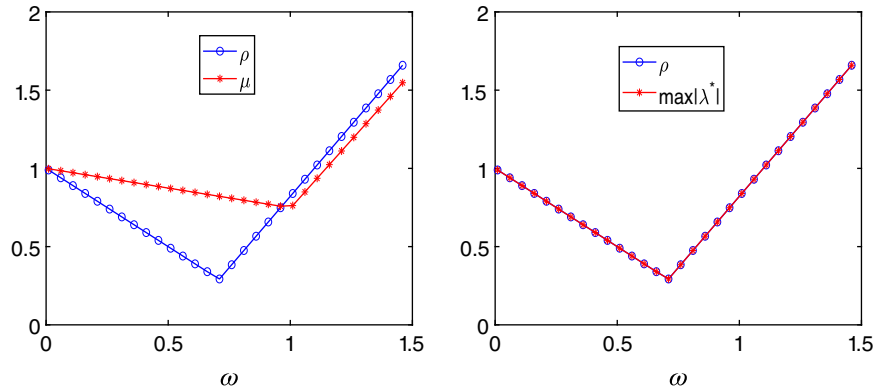
**TABLE 2** Two-grid and $V$-cycle convergence factors for the $Q_2$ approximation in one dimension with Jacobi weight $\omega^{***}$

| $\omega = \omega^{***} = \frac{56}{79} \approx 0.709, \mu = 0.822$ | | | |
|---|---|---|---|
| | $TG(1)$ | $TG(2)$ | $TG(3)$ | $TG(4)$ |
| $\rho$ | 0.291 | 0.249 | 0.090 | 0.064 |
| $\hat{\rho}_{h=1/128}$ | 0.291 | 0.249 | 0.089 | 0.064 |
| $\hat{\rho}_{h=1/256}$ | 0.291 | 0.249 | 0.089 | 0.064 |
| | $V(1)$ | $V(2)$ | $V(3)$ | $V(4)$ |
| $\hat{\rho}_{h=1/256}$ | 0.291 | 0.249 | 0.089 | 0.065 |

two-grid methods. This suggests that $V$ cycles can be of practical use and more expensive cycles, such as $F$- and $W$ cycles are not needed in this setting. Nonetheless, three-grid (or $k$-grid) LFA[5] could be applied to confirm that no degradation should be expected for $V$-cycles.

## 3.4 | A modified two-grid analysis

To better understand the failure of classical smoothing analysis for the $Q_2$ approximation, we first consider why the smoothing factor is a good predictor of performance for the $Q_1$ approximation. In the $Q_1$ case, we denote the CGC operator as $\hat{\mathcal{M}}_{1,h}^{\text{CGC}}(\theta)$, and the symbol of the relaxation scheme as $\hat{S}_{1,h}(\omega, \theta)$, which are both $2 \times 2$ matrices. Here we use linear interpolation for $P$ and $R = P^H$. By standard calculation, we have

$$\hat{\mathcal{M}}_{1,h}^{\text{CGC}}(\theta) = \begin{pmatrix} \sin^2(\frac{\theta}{2}) & \cos^2(\frac{\theta}{2}) \\ \sin^2(\frac{\theta}{2}) & \cos^2(\frac{\theta}{2}) \end{pmatrix}.$$

In the standard LFA smoothing analysis, rather than consider the true CGC, $\hat{\mathcal{M}}_{1,h}^{\text{CGC}}(\theta)$, we assume an "ideal" CGC operator, $\mathcal{Q}_h$, that annihilates the low-frequency error components and leaves the high-frequency components unchanged (see the work of Trottenberg et al.[7]). More precisely, for the $Q_1$ approximation to the Laplacian in 1D, $\mathcal{Q}_h$ is typically taken to be the projection matrix,

$$\begin{pmatrix} 0 & 0 \\ 0 & 1 \end{pmatrix}.$$

To compute the convergence factor, we replace the CGC operator in Equation (7) by $\mathcal{Q}_h$, giving

$$\tilde{\rho} := \sup \left\{ \rho(\mathcal{Q}_h \hat{S}_{1,h}(\omega, \theta)) : \theta \in \Theta_{2h} \right\}. \tag{24}$$

*Remark* 2. Note that Equation (24) is equivalent to form Equation (3).

From the form of $\mathcal{Q}_h$ we can consider optimizing the smoothing factor by working only over the high frequencies as in Definition 3. In Figure 4, we plot the LFA-predicted two-grid convergence factor (7) and the smoothing factor as a function of $\omega$ and see that the smoothing factor perfectly captures the LFA-predicted two-grid convergence behavior.

However, as shown above in Section 3.1, generalizing $\mathcal{Q}_h$ to

$$\begin{pmatrix} 0 & 0 & 0 & 0 \\ 0 & 0 & 0 & 0 \\ 0 & 0 & 1 & 0 \\ 0 & 0 & 0 & 1 \end{pmatrix},$$

does not give a good prediction of the two-grid convergence factor for the $Q_2$ approximation. Instead, we note that for the $Q_1$ case,

$$\lim_{\theta \to 0} \hat{\mathcal{M}}_{1,h}^{\text{CGC}}(\theta) = \begin{pmatrix} 0 & 1 \\ 0 & 1 \end{pmatrix},$$
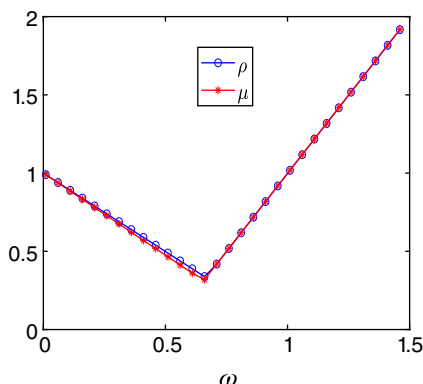


**FIGURE 4** Local Fourier analysis-predicted two-grid convergence and smoothing factors as a function of $\omega$ for the $Q_1$ approximation in one dimension

and, if we replace $Q_h$ by this limit, then the eigenvalues of $Q_h \hat{S}_{1,h}(\omega, \theta)$ do not change. This suggests that using $\lim_{\theta \to 0} \hat{\mathcal{M}}_{1,h}^{\mathrm{CGC}}(\theta)$ as the ideal CGC operator may improve the robustness of the smoothing factor in more complicated settings. We now extend this approximation for two-grid analysis of the $Q_2$ approximation.

Define

$$Q_0 := \lim_{\theta \to 0} \left( I - \hat{P}(\theta)(\tilde{A}_{2h}(2\theta))^{-1} \hat{R}(\theta) \hat{A}_h(\theta) \right). \tag{25}$$

By standard calculation,

$$Q_0 = \begin{pmatrix} \frac{1}{2} & -\frac{1}{2} & -\frac{1}{4} & 0 \\ -\frac{1}{4} & \frac{1}{4} & \frac{1}{8} & 0 \\ -\frac{1}{2} & \frac{1}{2} & \frac{1}{4} & 0 \\ 0 & 0 & 0 & 1 \end{pmatrix}.$$

To see how well $Q_0$ works as an idealized CGC operator when predicting the two-grid convergence factor, let

$$\rho_0 = \rho_0(\omega) = \sup \left\{ \rho(Q_0 \hat{S}_h(\omega, \theta)) : \theta \in \Theta_{2h} \right\}. \tag{26}$$

We plot $\rho_0$ as a function of $\omega$, compared with the LFA-predicted two-grid convergence factor, $\rho$, for the $Q_2$ discretization. Figure 5 shows that $\rho_0$ provides a much better prediction than the classical smoothing factor. Note that for smaller values of $\omega$, $\rho_0$ slightly overpredicts the convergence factor, as $Q_0$ captures poorly the true effects of CGC for values of $\theta$ near $\pm\frac{\pi}{2}$ (noting that for small $\omega$, $\rho_0(\omega) = \rho(Q_0 \hat{S}_h(\omega, \pm\frac{\pi}{2}))$), but that true two-grid performance is dominated by the $\theta = 0$ harmonic. We see that the optimal parameter for $\rho_0$ is very close to the optimal parameter for the two-grid convergence factor, $\rho$. Whether further improvement is possible is an open question.

We now consider a modified two-grid error-propagation operator,

$$\hat{\mathcal{M}}_h^{\mathrm{MTGM}}(\omega, \theta) := Q_0 \hat{S}_h(\omega, \theta), \theta \in \Theta_{2h},$$

which gives a good prediction for the convergence of multigrid for the $Q_2$ approximation. Now, we consider minimizing the spectral radius of $\hat{\mathcal{M}}_h^{\mathrm{MTGM}}(\omega, \theta)$; that is, to minimize $\rho_0$.

By standard calculation, we have

$$\hat{S}_h(\omega, \theta) = \begin{pmatrix} 1 - \omega(1 + \frac{\cos(\theta)}{7}) & \frac{8}{7}\cos(\frac{\theta}{2})\omega & 0 & 0 \\ \cos(\frac{\theta}{2})\omega & 1 - \omega & 0 & 0 \\ 0 & 0 & 1 - \omega(1 - \frac{\cos(\theta)}{7}) & -\frac{8}{7}\sin(\frac{\theta}{2})\omega \\ 0 & 0 & -\sin(\frac{\theta}{2})\omega & 1 - \omega \end{pmatrix}.$$

Because $Q_0$ has rank 2, $\hat{\mathcal{M}}_h^{\mathrm{MTGM}}(\omega, \theta)$ has at most rank 2. By a straightforward calculation (done using a computer algebra system), the four eigenvalues of $Q_0 \hat{S}_h(\omega, \theta)$ are given by

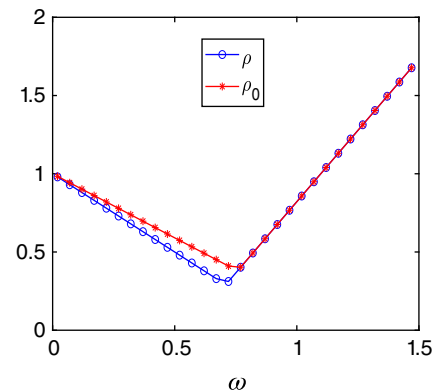$$\lambda(\theta) = 1 - g_{\pm}(\theta)\omega, 0, 0,$$



**FIGURE 5**  $\rho$ and $\rho_0$, as a function of $\omega$ for the $Q_2$ approximation in one dimension

where $g_\pm(\theta)$ is

$$\frac{112 + 44\cos(\frac{\theta}{2}) + 2\cos(\theta) \pm \sqrt{2\left(1381 + 44(\cos(\frac{\theta}{2}) + \cos(\frac{3\theta}{2})) - 412\cos(\theta) + \cos(2\theta)\right)}}{112}.$$

We can check that $g_\pm(\theta)$ is an increasing function over $[-\frac{\pi}{2}, 0]$ and a decreasing function over $[0, \frac{\pi}{2}]$. We plot $g_\pm(\theta)$ as a function of $\theta$ over $[-\frac{\pi}{2}, \frac{\pi}{2}]$ in Figure 6.

The extreme values of $g_\pm(\theta)$ are obtained at $\theta = 0$ and $\theta = \pm\frac{\pi}{2}$; that is,

$$g_+(0) = \frac{51}{28}, \quad g_-(0) = 1,$$

$$g_+(\pm\frac{\pi}{2}) = \frac{56 + 11\sqrt{2} + \sqrt{690}}{56} < \frac{51}{28},$$

$$g_-(\pm\frac{\pi}{2}) = \frac{56 + 11\sqrt{2} - \sqrt{690}}{56} < 1.$$

Thus,

$$\rho_0 = \sup\left\{\rho(\mathcal{Q}_0 \hat{S}_h(\omega, \theta)) : \theta \in \Theta_{2h}\right\} = \max\left\{\left|1 - \frac{51}{28}\omega\right|, \left|1 - g_-(\pm\frac{\pi}{2})\omega\right|\right\}.$$

Then, the optimal parameter minimizing $\rho_0$ is given by

$$\omega_{0,opt} = \frac{2}{\frac{51}{28} + \frac{56 + 11\sqrt{2} - \sqrt{690}}{56}} \approx 0.760,$$

and the corresponding predicted modified smoothing factor is

$$\rho_{0,opt} = \frac{\frac{51}{28} - \frac{56 + 11\sqrt{2} - \sqrt{690}}{56}}{\frac{51}{28} + \frac{56 + 11\sqrt{2} - \sqrt{690}}{56}} \approx 0.385.$$

Recall the optimal parameter and the true two-grid convergence factor are $\omega^{***} = 0.709$, $\rho = 0.291$, respectively. Compared with the true two-grid convergence, $\rho_0$ overpredicts the convergence factor based on the mode $\theta = \pm\frac{\pi}{2}$. However, this modified $\hat{\mathcal{M}}_h^{\text{MTGM}}(\omega, \theta)$ still offers useful information and a reasonable predictor of performance. Whether this "ideal" predictor can be used for other higher-order finite-element approximations will be explored in the following sections.

*Remark* 3. Improved two-grid behavior can be achieved by considering different weights for the DOFs at nodes and those at cell centers for Jacobi relaxation; that is, putting distinct parameters in each diagonal block in the diagonal operator in Equation (10). The LFA shown above can be extended to this relaxation scheme to optimize the two-grid convergence factor, resulting in somewhat better convergence.
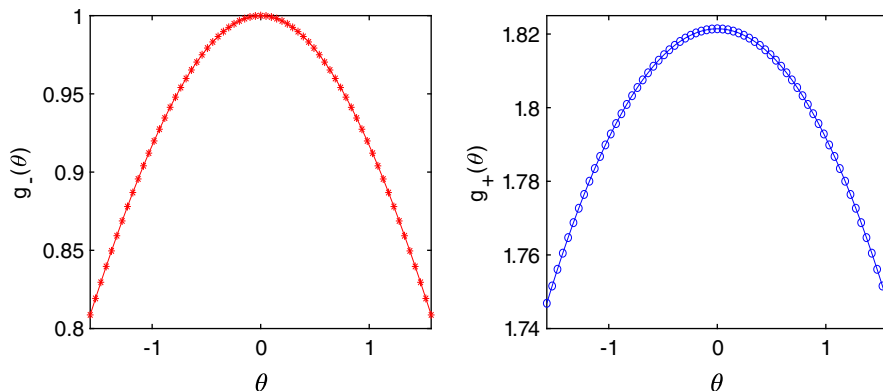


**FIGURE 6** At left, $g_-(\theta)$ as a function of $\theta$. At right, $g_+(\theta)$ as a function of $\theta$

*Remark* 4. There are different choices of basis for the $Q_2$ finite-element space and each has a natural (but different) quadratic interpolation operator. Consequently, the two-grid error-propagation operator (and LFA representation) depends on the choice of the basis for $Q_2$. This will affect the optimal choice of parameters and the resulting performance of the two-grid method. Note that there already exist some studies of the influence of the grid-transfer operators on multigrid performance.[9,36] Here, we consider only the standard basis for $Q_2$ as presented above. However, the analysis presented here can easily be extended to other finite-element bases and other grid-transfer operators.

## 4 | HIGHER-ORDER FINITE-ELEMENT METHODS

In this section, we consider the finite-element spaces $Q_k$ for $k = 3, 4$ and again examine the relationship between the LFA smoothing and two-grid convergence factors. In order to distinguish the block symbols for different $k$, we use superscripts in the matrices and block symbols in this section.

### 4.1 | Cubic Lagrangian elements

For cubic Lagrangian elements ($Q_3$), using nodal finite-element basis functions defined at the mesh nodes and the 1/3 and 2/3 points of the element, the elementary contributions to the stiffness matrix can be written as

$$
\text{EK}_h^{(3)} = \frac{1}{40h} \begin{pmatrix} 296 & -189 & 54 & -13 \\ -189 & 432 & -297 & 54 \\ 54 & -297 & 432 & -189 \\ -13 & 54 & -189 & 296 \end{pmatrix}.
$$

The corresponding symbol of stiffness operator is

$$
\tilde{A}_h^{(3)}(\theta) = \frac{1}{h} \begin{pmatrix} \frac{148-13\cos\theta}{20} & \frac{54e^{-\frac{2}{3}i\theta}-189e^{\frac{1}{3}i\theta}}{40} & \frac{54e^{\frac{2}{3}i\theta}-189e^{-\frac{1}{3}i\theta}}{40} \\ \frac{54e^{\frac{2}{3}i\theta}-189e^{-\frac{1}{3}i\theta}}{40} & \frac{54}{5} & -\frac{297e^{\frac{1}{3}i\theta}}{40} \\ \frac{54e^{-\frac{2}{3}i\theta}-189e^{\frac{1}{3}i\theta}}{40} & -\frac{297e^{-\frac{1}{3}i\theta}}{40} & \frac{54}{5} \end{pmatrix},
$$

ordered as mesh nodes, then the 1/3 points and 2/3 points, respectively. The error-propagation symbol of weighted Jacobi relaxation is given by

$$
\tilde{S}_h^{(3)}(\omega, \theta) = I - \omega \left( \tilde{M}_h^{(3)}(\theta) \right)^{-1} \tilde{A}_h^{(3)}(\theta), \tag{27}
$$

where

$$
\tilde{M}_h^{(3)}(\theta) = \frac{1}{h} \begin{pmatrix} \frac{37}{5} & 0 & 0 \\ 0 & \frac{54}{5} & 0 \\ 0 & 0 & \frac{54}{5} \end{pmatrix}.
$$

In Figure 7, we plot the eigenvalues of $\left( \tilde{M}_h^{(3)}(\theta) \right)^{-1} \tilde{A}_h^{(3)}(\theta)$. Considering the high frequencies, we see $\lambda_{\min,H} = 0.085$ is obtained at $\theta = \frac{\pi}{2}$, and $\lambda_{\max,H} = 2.394$ is obtained at $\theta = \pi$.

Thus, the classical optimal choice of $\omega$ for Equation (27) is given by

$$
\omega_3^* = \frac{2}{\lambda_{\min,H} + \lambda_{\max,H}} = 0.807,
$$

and

$$
\mu_3^* = \min_{\omega} \max_{\theta \in T^{\text{high}}} \left| \lambda(\tilde{S}_h^{(3)}(\omega, \theta)) \right| = \frac{\lambda_{\max,H} - \lambda_{\min,H}}{\lambda_{\max,H} + \lambda_{\min,H}} \approx 0.931.
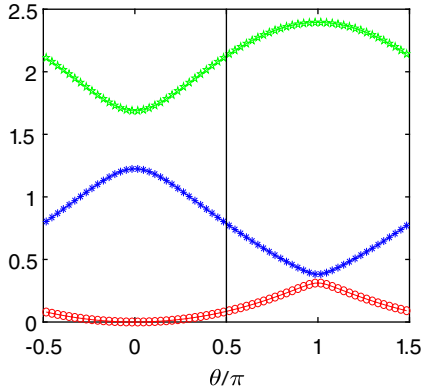$$

**FIGURE 7**  The distribution of eigenvalues of $\left(\tilde{M}_h^{(3)}(\theta)\right)^{-1}\tilde{A}_h^{(3)}(\theta)$ as a function of $\theta/\pi$

Denote the cubic finite-element restriction operator as $R^{(3)}$ and the corresponding symbol as $\tilde{R}^{(3)}(\theta)$. Similarly to Theorem 1, we can write the symbol of restriction, $R^{(3)}$, as

$$\tilde{R}^{(3)}(\theta^\alpha) = \begin{pmatrix} 1 - \frac{e^{\iota\theta^\alpha}}{16} - \frac{e^{-\iota\theta^\alpha}}{16} & \frac{5}{16}e^{\frac{1}{3}\iota\theta^\alpha} + \frac{1}{16}e^{-\frac{5}{3}\iota\theta^\alpha} & \frac{5}{16}e^{-\frac{1}{3}\iota\theta^\alpha} + \frac{1}{16}e^{\frac{5}{3}\iota\theta^\alpha} \\ \frac{9}{16}e^{\frac{1}{3}\iota\theta^\alpha}\beta & \frac{15}{16}e^{-\frac{1}{3}\iota\theta^\alpha}\beta & (1 - \frac{5}{16}e^{\iota\theta^\alpha})\beta \\ \frac{9}{16}e^{-\frac{1}{3}\iota\theta^\alpha}\beta^2 & (1 - \frac{5}{16}e^{-\iota\theta^\alpha})\beta^2 & \frac{15}{16}e^{\frac{1}{3}\iota\theta^\alpha}\beta^2 \end{pmatrix},$$

where $\beta = (e^{\frac{2}{3}\iota\pi})^\alpha$. Thus, the symbol of $R^{(3)}$ is the $3 \times 6$ matrix

$$\hat{R}^{(3)}(\theta) = \left(\tilde{R}^{(3)}(\theta^0) \ \tilde{R}^{(3)}(\theta^1)\right), \text{ where } \theta = \theta^0 \in \Theta_{2h}.$$

The Fourier representation of $P^{(3)}$ is given by the $6 \times 3$ matrix,

$$\hat{P}^{(3)}(\theta) = \frac{1}{2}\left(\hat{R}^{(3)}(\theta)\right)^H.$$

We plot the smoothing factor and LFA-predicted two-grid convergence factor as a function of $\omega$ for cubic elements in 1D. Figure 8 indicates that when the smoothing factor achieves its optimal value, the corresponding $\omega$ does not minimize the two-grid convergence factor. From Figure 8, note that the optimal convergence factor, $\rho$, is 0.491 with $\omega = 0.650$, but the corresponding smoothing factor is 0.943, which is larger than the smoothing factor of 0.931 for $\omega_3^* = 0.807$ given above.

As the LFA smoothing factor again fails to predict the convergence factor, we extend the modification above to yield a new prediction based on $\hat{\mathcal{M}}_h^{\text{MTGM}}(\omega, \theta)$, calculating $\mathcal{Q}_0$ again using the limit in Equation (25). We plot $\rho_0$, compared with the true convergence factor at the right of Figure 8, and see that using $\mathcal{Q}_0$ accurately predicts the true convergence factor, except for a small overestimate for $\omega$ less than 0.65, as $\mathcal{Q}_0$ captures poorly the true effects of CGC for values of $\theta$ near $\pm\frac{\pi}{2}$. We observe that when $\theta = 0$, $\rho_0$ underestimates the true two-grid convergence factor. However, the optimal parameter of $\hat{\mathcal{M}}_h^{\text{MTGM}}(\omega, \theta)$ is very close to the true optimal parameter for the two-grid convergence factor.
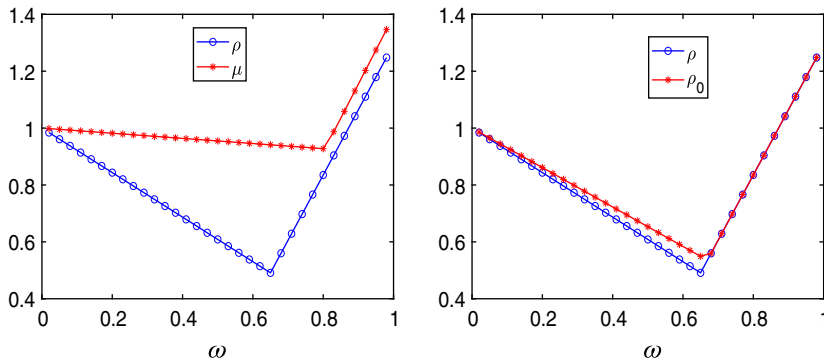


**FIGURE 8**  At left, the local Fourier analysis-predicted two-grid convergence and smoothing factors as a function of $\omega$. At right, $\rho$ and $\rho_0$ as a function of $\omega$ for the $Q_3$ approximation in one dimension

**TABLE 3** Local Fourier analysis predictions for the $Q_3$ approximation in one dimension

| | $\omega = \omega_3^* = 0.807, \mu = 0.932$ | | | | $\omega = \omega_{opt} = 0.650, \mu = 0.943$ | | | |
| --- | --- | --- | --- | --- | --- | --- | --- | --- |
| | $TG(1)$ | $TG(2)$ | $TG(3)$ | $TG(4)$ | $TG(1)$ | $TG(2)$ | $TG(3)$ | $TG(4)$ |
| $\rho$ | 0.852 | 0.842 | 0.749 | 0.721 | 0.491 | 0.337 | 0.151 | 0.131 |
| $\rho_0$ | 0.852 | 0.842 | 0.749 | 0.721 | 0.553 | 0.346 | 0.233 | 0.187 |
| $\hat{\rho}_{h=1/128}$ | 0.852 | 0.842 | 0.748 | 0.721 | 0.491 | 0.336 | 0.150 | 0.130 |
| $\hat{\rho}_{h=1/256}$ | 0.851 | 0.842 | 0.749 | 0.721 | 0.491 | 0.336 | 0.150 | 0.130 |

In Table 3, we show LFA predictions and measured two-grid performance with different choices of parameter, taking $\omega_{opt}$ from Figure 8 as the point where the modified smoothing factor is minimized. We see the optimal parameter, $\omega_3^*$, corresponding to the classical smoothing factor is not a good choice for optimizing the two-grid convergence factor, but $\omega_{opt}$ is confirmed as a good choice of parameter by both the LFA two-grid convergence factor and our modified predictions.

## 4.2 | Quartic Lagrangian elements

For quartic Lagrangian elements ($Q_4$), using nodal finite-element basis functions defined at the mesh nodes and the $1/4, 1/2$, and $3/4$ points of the element, the elementary contributions to the stiffness matrix can be written as

$$EK_h^{(4)} = \frac{1}{945h} \begin{pmatrix} 9850 & -6848 & 3048 & -1472 & 347 \\ -6848 & 16640 & -14208 & 5888 & -1472 \\ 3048 & -14208 & 22320 & -14208 & 3048 \\ -1472 & 5888 & -14208 & 16640 & -6848 \\ 347 & -1472 & 3048 & -6848 & 9850 \end{pmatrix},$$

and the corresponding symbol of stiffness operator is

$$\tilde{A}_h^{(4)}(\theta) = \frac{1}{h} \begin{pmatrix} \frac{9850+347(\eta^{-4}+\eta^4)}{945} & -\frac{6848\eta+1472\eta^{-3}}{945} & \frac{1016\eta^{-2}+1016\eta^2}{315} & -\frac{6848\eta^{-1}+1472\eta^3}{945} \\ -\frac{6848\eta^{-1}+1472\eta^3}{945} & \frac{3328}{189} & -\frac{4736\eta}{315} & \frac{5888\eta^2}{945} \\ \frac{1016\eta^2+1016\eta^{-2}}{315} & -\frac{4736\eta^{-1}}{315} & \frac{496}{21} & -\frac{4736\eta}{315} \\ -\frac{6848\eta+1472\eta^{-3}}{945} & \frac{5888\eta^{-2}}{945} & -\frac{4736\eta^{-1}}{315} & \frac{3328}{189} \end{pmatrix},$$

where $\eta = e^{\frac{i\theta}{4}}$, with both ordered as mesh nodes, then the $1/4, 1/2$, and $3/4$ points of the mesh (followed by the right-hand node in $EK_h^{(4)}$).

The error-propagation symbol of weighted Jacobi relaxation is

$$\tilde{S}_h^{(4)}(\omega, \theta) = I - \omega \left( \tilde{M}_h^{(4)}(\theta) \right)^{-1} \tilde{A}_h^{(4)}(\theta),$$

where

$$\tilde{M}_h^{(4)}(\theta) = \frac{1}{h} \begin{pmatrix} \frac{1970}{189} & 0 & 0 & 0 \\ 0 & \frac{3328}{189} & 0 & 0 \\ 0 & 0 & \frac{496}{21} & 0 \\ 0 & 0 & 0 & \frac{3328}{189} \end{pmatrix}.$$

Using these symbols, we plot the distribution of eigenvalues of $\left( \tilde{M}_h^{(4)}(\theta) \right)^{-1} \tilde{A}_h^{(4)}(\theta)$ in Figure 9. From Figure 9, we see that the smallest eigenvalue over the high frequencies, $\lambda_{min,H} = 0.036$ is obtained at $\theta = \frac{\pi}{2}$ or $\frac{3\pi}{2}$. Similarly, $\lambda_{max,H} = 2.557$ is achieved with $\theta = \frac{\pi}{2}$ or $\frac{3\pi}{2}$.
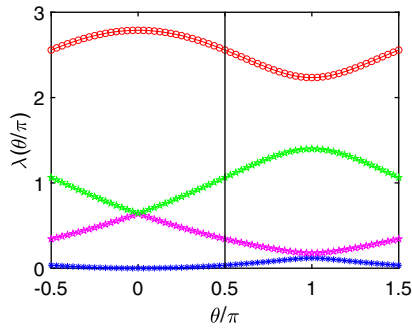
**FIGURE 9**  The distribution of eigenvalues of $\left(\tilde{M}_h^{(4)}(\theta)\right)^{-1}\tilde{A}_h^{(4)}(\theta)$ as a function of $\theta/\pi$

Thus, the optimal $\omega$ for the classical smoothing factor and the corresponding smoothing factor are

$$\omega_4^* = \frac{2}{\lambda_{\min,H} + \lambda_{\max,H}} = 0.772, \quad \mu_4^* = 0.973, \tag{28}$$

respectively.

As in the $Q_2$ case, the biggest eigenvalue over all frequencies is $\lambda_{\max}^* = 2.789 > \lambda_{\max,H}$, obtained at $\theta = 0$. We, thus, consider the case of

$$\omega_4^{**} = \frac{2}{\lambda_{\min,H} + \lambda_{\max}^*} = 0.708.$$

Then, the corresponding smoothing factor is

$$\mu_4^{**} = \max_{\theta \in T^{\text{high}}} \left|\lambda(\tilde{S}_h^{(4)}(\omega^{**}, \theta))\right| = \frac{\lambda_{\max}^* - \lambda_{\min,H}}{\lambda_{\max}^* + \lambda_{\min,H}} = 0.975. \tag{29}$$

Denote the quartic restriction operator as $R^{(4)}$ and the corresponding symbol as $\tilde{R}^{(4)}(\theta)$. Similarly to Theorem 1, we can write the symbol of restriction, $R^{(4)}$, as

$$\tilde{R}^{(4)}(\theta^\alpha) = \begin{pmatrix} 1 & \frac{35}{128}\xi + \frac{3}{128}\xi^5 - \frac{5}{128}\xi^{-7} - \frac{5}{128}\xi^{-3} & 0 & \frac{35}{128}\xi^{-1} + \frac{3}{128}\xi^{-5} - \frac{5}{128}\xi^7 - \frac{5}{128}\xi^3 \\ 0 & (\frac{35}{32}\xi^{-1} - \frac{5}{32}\xi^3)\gamma & \gamma & (\frac{15}{32}\xi + \frac{7}{32}\xi^5)\gamma \\ \gamma^2 & (-\frac{35}{64}\xi^{-3} + \frac{45}{64}\xi)\gamma^2 & 0 & (\frac{45}{64}\xi^{-1} - \frac{35}{64}\xi^3)\gamma^2 \\ 0 & (\frac{7}{32}\xi^{-5} + \frac{15}{32}\xi^{-1})\gamma^3 & \gamma^3 & (-\frac{5}{32}\xi^{-3} + \frac{35}{32}\xi)\gamma^3 \end{pmatrix},$$

where $\xi = e^{\frac{\imath\theta^\alpha}{4}}, \gamma = (e^{\frac{1}{2}\imath\pi})^\alpha$. Thus, the symbol of $R^{(4)}$ is the $4 \times 8$ matrix

$$\hat{R}^{(4)}(\theta) = \left(\tilde{R}^{(4)}(\theta^0) \ \tilde{R}^{(4)}(\theta^1)\right), \text{ where } \theta = \theta^0 \in \Theta_{2h}.$$

The Fourier representation of $P^{(4)}$ is given by the $8 \times 4$ matrix,

$$\hat{P}^{(4)}(\theta) = \frac{1}{2}\left(\hat{R}^{(4)}(\theta)\right)^H.$$

We plot the LFA smoothing and two-grid convergence factors as a function of $\omega$ for this algorithm. At the left of Figure 10, we see that the LFA smoothing factor again fails to predict the two-grid convergence factor, and that the optimal convergence factor $\rho$ is 0.608 with $\omega = 0.640$. The choices of $\omega$ in Equations (28) and (29) both fail.

We present the results of the modified prediction using $\hat{\mathcal{M}}_h^{\text{MTGM}}(\omega, \theta)$ here again defining $Q_0$ following Equation (25). At the right of Figure 10, we compare $\rho_0$ with $\rho$, as a function of the relaxation parameter, $\omega$, seeing that $\rho_0$ matches well with the true convergence, except for a small overestimation for small $\omega$, as $Q_0$ captures poorly the true effects of CGC for values of $\theta$ near $\pm\frac{\pi}{2}$. We also observe that when $\theta = 0$, $\rho_0$ is exactly the true two-grid convergence factor, which is the same as in the case of the $Q_2$ approximation.

**FIGURE 10** At left, local Fourier analysis-predicted two-grid convergence and smoothing factors as a function of $\omega$. At right, $\rho$ and $\rho_0$ as a function of $\omega$ for the $Q_4$ approximation in one dimensions
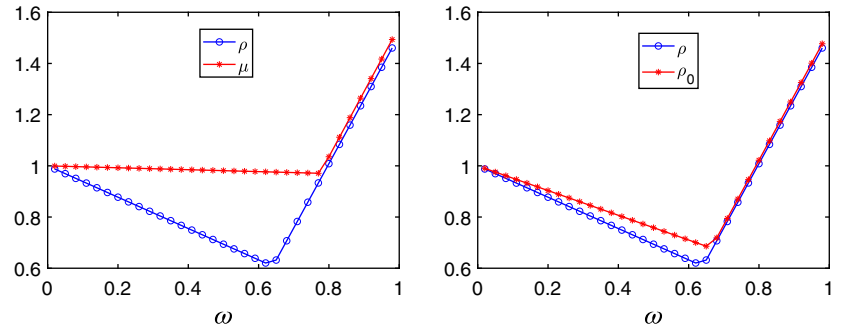


**TABLE 4** Local Fourier analysis predictions for the $Q_4$ approximation in one dimension

| | $\omega = \omega_4^* = 0.772, \mu = 0.972$ | | | | $\omega = \omega_4^{**} = 0.708, \mu = 0.974$ | | | | $\omega = \omega_{opt} = 0.640, \mu = 0.976$ | | | |
|---|---|---|---|---|---|---|---|---|---|---|---|---|
| | $TG(1)$ | $TG(2)$ | $TG(3)$ | $TG(4)$ | $TG(1)$ | $TG(2)$ | $TG(3)$ | $TG(4)$ | $TG(1)$ | $TG(2)$ | $TG(3)$ | $TG(4)$ |
| $\rho$ | 0.938 | 1.136 | 1.267 | 1.481 | 0.778 | 0.825 | 0.758 | 0.762 | 0.608 | 0.559 | 0.388 | 0.331 |
| $\rho_0$ | 0.951 | 1.136 | 1.267 | 1.481 | 0.790 | 0.825 | 0.758 | 0.762 | 0.693 | 0.564 | 0.407 | 0.342 |
| $\hat{\rho}_{h=1/256}$ | 0.938 | 1.135 | 1.266 | 1.480 | 0.777 | 0.825 | 0.758 | 0.761 | 0.607 | 0.558 | 0.388 | 0.330 |

In Table 4, we show LFA predictions and measured two-grid convergence factors with different choices of the relaxation parameter, where $\omega_{opt}$ is chosen numerically to minimize the modified smoothing factor. Even though the smoothing factors are similar with these three parameters, the two-grid convergence shows different behavior. We see the parameters $\omega_4^*$ and $\omega_4^{**}$ are not good choices to obtain the optimal two-grid convergence factor, while $\omega_{opt}$ demonstrates the effectiveness of our modified predictions.

## 5 | LFA FOR THE $Q_2$ APPROXIMATION IN 2D

In this section, we consider LFA for problem (1) in 2D, using biquadratic finite elements and nodal basis functions defined at the mesh nodes, edge midpoints and element centers. We order the DOFs of the $Q_2$ approximation as nodes first, then midpoints of the edges parallel to the $x$-axis (the "$x$-edges"), followed by the midpoints of the edges parallel to the $y$-axis (the "$y$-edges"), and then the element centers. In this way, the grids in 2D are defined as

$$\boldsymbol{G_h} = G_{h_x} \oplus G_{h_y},$$

where

$$\boldsymbol{x} := (x, y) \in \boldsymbol{G_h} \text{ if and only if } x \in G_{h_x} \text{ and } y \in G_{h_y},$$

where $G_{h_x}$ and $G_{h_y}$ are defined as in 1D, see Equation (4). Here, we consider $h_x = h_y = h$.

Thus, $\boldsymbol{G_h}$ can be rewritten as $\boldsymbol{G_h} = \boldsymbol{G}_h^1 \cup \boldsymbol{G}_h^2 \cup \boldsymbol{G}_h^3 \cup \boldsymbol{G}_h^4$ with

$$\boldsymbol{G}_h^j = \begin{cases} G_{h,N} \oplus G_{h,N} & \text{if } j = 1, \\ G_{h,C} \oplus G_{h,N} & \text{if } j = 2, \\ G_{h,N} \oplus G_{h,C} & \text{if } j = 3, \\ G_{h,C} \oplus G_{h,C} & \text{if } j = 4. \end{cases}$$

We refer to $\boldsymbol{G}_h^1, \boldsymbol{G}_h^2, \boldsymbol{G}_h^3,$ and $\boldsymbol{G}_h^4$ as the *NN*-, *CN*-, *NC*-, and *CC*-type points on the grid $\boldsymbol{G_h}$, respectively.

### 5.1 | Representation of the stiffness and mass operators

It is known that the stiffness and mass matrices for the $Q_1$ approximation in 2D can be written using tensor products of their 1D analogues. However, for the $Q_2$ approximation in 2D, we must carefully consider the ordering of the DOFs and

the block structure of the resulting system. Assume that the stiffness and mass matrices in 1D are ordered by nodes and centers in $2 \times 2$-block matrices, given by

$$\mathcal{A}^{(2)} = \begin{pmatrix} A_{nn} & A_{nc} \\ A_{cn} & A_{cc} \end{pmatrix}, \quad \mathcal{B}^{(2)} = \begin{pmatrix} B_{nn} & B_{nc} \\ B_{cn} & B_{cc} \end{pmatrix},$$

respectively. For the 2D case, we use the Tracy-Singh product to preserve block structuring in the product. Let $\mathbf{A}$ be an $(s \times t)$-block matrix, whose $(i,j)$-block is denoted by $A_{ij}$, and $\mathbf{B}$ be a $(p \times q)$-block matrix, whose $(i,j)$-block is denoted by $B_{ij}$. The Tracy–Singh product of $\mathbf{A}$ and $\mathbf{B}$ is defined by the pairwise Kronecker product for each pair of blocks in matrices $\mathbf{A}$ and $\mathbf{B}$, that is,

$$\mathbf{A} \circ \mathbf{B} = \begin{pmatrix} A_{11} \bar{\otimes} \mathbf{B} & \dots & A_{1t} \bar{\otimes} \mathbf{B} \\ \vdots & \ddots & \vdots \\ A_{s1} \bar{\otimes} \mathbf{B} & \dots & A_{st} \bar{\otimes} \mathbf{B} \end{pmatrix}, \text{where } A_{i,j} \bar{\otimes} \mathbf{B} = \begin{pmatrix} A_{ij} \otimes B_{11} & \dots & A_{ij} \otimes B_{1q} \\ \vdots & \ddots & \vdots \\ A_{ij} \otimes B_{p1} & \dots & A_{ij} \otimes B_{pq} \end{pmatrix},$$

and $\otimes$ is the standard Kronecker product. Then, the stiffness and mass matrices in 2D are given by

$$\mathcal{A}_2 = \mathcal{A}^{(2)} \circ \mathcal{B}^{(2)} + \mathcal{B}^{(2)} \circ \mathcal{A}^{(2)}, \quad \mathcal{B}_2 = \mathcal{B}^{(2)} \circ \mathcal{B}^{(2)},$$

respectively, and the ordering of the $4 \times 4$ block system corresponds to the indexing of the $\mathbf{G}_h^j$ given above. Similarly, if the quadratic restriction matrix in 1D is given in block form as

$$\mathcal{R}^{(2)} = \begin{pmatrix} R_{nn} & R_{nc} \\ R_{cn} & R_{cc} \end{pmatrix},$$

then the corresponding restriction matrix in 2D is given by

$$\mathcal{R}_2 = \mathcal{R}^{(2)} \circ \mathcal{R}^{(2)},$$

with the same block ordering as the blocks in $\mathcal{A}_2$.

Using the Tracy–Singh product for the discretized operators allows us to compute symbols using standard Kronecker products. Given the symbols of the stiffness and mass operators for the $Q_2$ approximation in 1D, $\tilde{A}_h(\theta)$ and $\tilde{B}_h(\theta)$, respectively, the symbols of the stiffness and mass matrices in 2D are given by

$$\tilde{A}_2(\theta_1, \theta_2) = \tilde{A}_h(\theta_2) \otimes \tilde{B}_h(\theta_1) + \tilde{B}_h(\theta_2) \otimes \tilde{A}_h(\theta_1),$$
$$\tilde{B}_2(\theta_1, \theta_2) = \tilde{B}_h(\theta_2) \otimes \tilde{B}_h(\theta_1),$$

respectively. The above discussion is not limited to $Q_2$, and extends to $Q_k$ as follows.

*Remark* 5. The stiffness and mass matrices for the $Q_k$ discretization in 2D can be written as

$$\mathcal{A}_k = \mathcal{A}^{(k)} \circ \mathcal{B}^{(k)} + \mathcal{B}^{(k)} \circ \mathcal{A}^{(k)}, \mathcal{B}_k = \mathcal{B}^{(k)} \circ \mathcal{B}^{(k)},$$

respectively, where $\mathcal{A}^{(k)}$ and $\mathcal{B}^{(k)}$ are stiffness and mass matrices for the $Q_k$ discretization in 1D, respectively.

*Remark* 6. The symbols of the stiffness and mass matrices for the $Q_k$ discretization in 2D are as follows

$$\tilde{A}_k(\theta_1, \theta_2) = \tilde{A}_h^{(k)}(\theta_2) \otimes \tilde{B}_h^{(k)}(\theta_1) + \tilde{B}_h^{(k)}(\theta_2) \otimes \tilde{A}_h^{(k)}(\theta_1),$$
$$\tilde{B}_k(\theta_1, \theta_2) = \tilde{B}_h^{(k)}(\theta_2) \otimes \tilde{B}_h^{(k)}(\theta_1),$$

respectively, where $\tilde{A}_h^{(k)}(\theta)$ and $\tilde{B}_h^{(k)}(\theta)$ are the stiffness and mass symbols for the $Q_k$ discretization in 1D, respectively.

*Remark* 7. The restriction matrix corresponding to the $Q_k$ approximation in 2D is given by

$$\mathcal{R}_k = \mathcal{R}^{(k)} \circ \mathcal{R}^{(k)},$$

with the same block ordering as $\mathcal{A}_k$ if $\mathcal{R}^{(k)}$ is ordered consistently with $\mathcal{A}^{(k)}$.

## 5.2 | Fourier representation of grid transfer operators

Now we turn to the representation of biquadratic interpolation and its adjoint operator, restriction, in 2D. The extension of the restriction operator given in Equations (17) and (18) from 1D to 2D with blocks ordered as mesh nodes, $x$-edge midpoints, $y$-edge midpoints, and cell centers can be written as $R = \{R_{NN}, R_{CN}, R_{NC}, R_{CC}\}$, respectively. Let $\tilde{R}_{NN}, \tilde{R}_{CN}, \tilde{R}_{NC}$, and $\tilde{R}_{CC}$ be their Fourier representations. We show the representation of transfer operators is given by tensor products of their symbols in 1D.

Let

$$\alpha = (\alpha_1, \alpha_2) \in \{(0,0), (1,0), (0,1), (1,1)\},$$
$$\theta^\alpha = (\theta_1^{\alpha_1}, \theta_2^{\alpha_2}) = (\theta_1 + \alpha_1 \pi, \theta_2 + \alpha_2 \pi), \theta := \theta^{(0,0)}.$$

We use the ordering of $\alpha = (0,0), (1,0), (0,1), (1,1)$ for the four harmonics.

**Definition 6.** Assume that $T = [t_{\kappa_1}]$ and $S = [s_{\kappa_2}]$ are two stencil operators in 1D. The 2D stencil $S \otimes T$ is given by

$$S \otimes T := [r_\kappa]_h, \text{with } r_\kappa = t_{\kappa_1} s_{\kappa_2}, \text{and } \kappa = (\kappa_1, \kappa_2),$$

so that $R$ is the outer product of $S$ and $T$.

We use this outer-product notation to simplify the computation of the symbol of the restriction operator in block form. Rewrite Equations (17) and (18) as

$$R_N = \left[ -\frac{1}{8} \quad 0 \quad \frac{3}{8} \quad 1(\star) \quad \frac{3}{8} \quad 0 \quad -\frac{1}{8} \right], \tag{30}$$

and

$$R_C = \left[ \frac{3}{4} \quad 1(\star) \quad \frac{3}{4} \right], \tag{31}$$

respectively, by discarding the points outside the stencil of restriction. Then, the four restriction stencils in 2D for the $Q_2$ approximation can be denoted by

$$R_{I_x I_y} = R_{I_y} \otimes R_{I_x} := [r_\kappa]_{I_x I_y}, \tag{32}$$

where $I_x, I_y \in \{N, C\}$.

We can extend Definition 5 to a "standard" restriction operator in 2D as follows.

**Definition 7.** Let $T(\theta^\alpha) = [t_\kappa]$ be a restriction stencil in 2D given as $T = \mathcal{T}_2 \otimes \mathcal{T}_1$. We call

$$\tilde{T}(\theta^\alpha) = \sum_{\kappa \in V} t_\kappa e^{\iota \kappa \cdot \theta^\alpha} e^{\iota \pi \alpha \cdot x/h} := \sum_{\kappa \in V} \tilde{t}_\kappa = \sum_{(\kappa_1, \kappa_2) \in V} \tilde{t}_{\kappa_1} \tilde{t}_{\kappa_2}, \tag{33}$$

the restriction symbol of $T$.

Again, we emphasize that the appearance of $x$ in Equation (33) serves only to emphasize that the restriction symbol depends on the type of DoF to which we restrict, as Definition 5 and Remark 1. Here, by "standard," we mean the restriction operator is associated with only one type of meshpoint.

*Remark* 8. It is easy to check that, in Equation (33),

$$\tilde{T}(\theta^\alpha) = \sum_{(\kappa_1, \kappa_2) \in V} \tilde{t}_{\kappa_1} \tilde{t}_{\kappa_2} = \sum_{\kappa_1} \sum_{\kappa_2} \tilde{t}_{\kappa_1} \tilde{t}_{\kappa_2} = \tilde{\mathcal{T}}_1(\theta_1^{\alpha_1}) \tilde{\mathcal{T}}_2(\theta_2^{\alpha_2}),$$

where $\tilde{\mathcal{T}}_1(\theta_1^{\alpha_1})$ and $\tilde{\mathcal{T}}_2(\theta_2^{\alpha_2})$ are the restriction symbols for $\mathcal{T}_1$ and $\mathcal{T}_2$, respectively, due to the tensor product of $\mathcal{T}_2 \otimes \mathcal{T}_1$.

Note that $\boldsymbol{R}_{I_x I_y}$ draws values from four types of meshpoints on the fine grid. Similarly to 1D, the stencil $\boldsymbol{R}_{I_x I_y}$ can be split into four types of substencils, and the Fourier representation of $\boldsymbol{R}_{I_x I_y}$ can be written as a $(1 \times 4)$-matrix as follows,

$$\tilde{\boldsymbol{R}}_{I_x I_y}(\boldsymbol{\theta}^{\alpha}) = \left( \tilde{R}_{I_x I_y, NN}(\boldsymbol{\theta}^{\alpha}) \ \tilde{R}_{I_x I_y, CN}(\boldsymbol{\theta}^{\alpha}) \ \tilde{R}_{I_x I_y, NC}(\boldsymbol{\theta}^{\alpha}) \ \tilde{R}_{I_x I_y, CC}(\boldsymbol{\theta}^{\alpha}) \right). \tag{34}$$

The subscript $J_x J_y$ of $\tilde{R}_{I_x I_y, J_x J_y}(\boldsymbol{\theta}^{\alpha})$ ($J_x, J_y \in \{N, C\}$) denotes the contributions of the $J_x J_y$-type points on the fine grid to the $I_x I_y$ points on the coarse grid.

Thus, we can use Definition 7 to calculate $\tilde{R}_{I_x I_y, J_x J_y}(\boldsymbol{\theta}^{\alpha})$.

**Theorem 3.** *The entries in $\tilde{\boldsymbol{R}}_{I_x I_y}(\boldsymbol{\theta}^{\alpha})$ in Equation (34) are given by,*

$$\tilde{R}_{I_x I_y, J_x J_y}(\boldsymbol{\theta}^{\alpha}) = \tilde{R}_{I_y}(J_y, \theta_2^{\alpha_2}) \tilde{R}_{I_x}(J_x, \theta_1^{\alpha_1}), \tag{35}$$

*where $I_x, I_y, J_x, J_y \in \{N, C\}$. Note that the notation for the right-hand side of Equation (35) is defined in the proof of Theorem 1.*

*Proof.* Consider a 2D Fourier mode with frequency $\boldsymbol{\theta}^{\alpha}$, restricted to the coarse grid by the tensor product restriction operators given in Equation (32). Because $\boldsymbol{R}_{I_x I_y} = R_{I_y} \otimes R_{I_x}$, $\boldsymbol{R}_{I_x I_y}$ can be split into four substencils $R_{I_x I_y, J_x J_y}$, where $J_x, J_y \in \{N, C\}$, with corresponding symbol $\tilde{R}_{I_x I_y, J_x J_y}(\boldsymbol{\theta}^{\alpha})$. Since the tensor product preserves the stencil structure, $R_{I_x I_y, J_x J_y} = R_{I_y}(J_y) \otimes R_{I_x}(J_x)$, where $R_{I_y}(J_y)$ stands for the substencil of $R_{I_y}$ corresponding to the contributions from $J_y$-type points on the fine grid, see Equations (19) and (20). Thus, $\tilde{R}_{I_x I_y, J_x J_y}(\boldsymbol{\theta}^{\alpha})$ can be calculated based on Definition 7. According to Remark 8, $\tilde{R}_{I_x I_y, J_x J_y}(\boldsymbol{\theta}^{\alpha}) = \tilde{R}_{I_x}(J_x, \theta_1^{\alpha_1}) \tilde{R}_{I_y}(J_y, \theta_2^{\alpha_2})$. ∎

**Corollary 2.** *The symbol of restriction in 2D can be written as a tensor product of the restriction symbol, $\tilde{R}(\theta^{\alpha})$, in 1D, that is, $\tilde{\boldsymbol{R}}(\boldsymbol{\theta}^{\alpha})$ is the $4 \times 4$-matrix given by*

$$\tilde{\boldsymbol{R}}(\boldsymbol{\theta}^{\alpha}) = \tilde{R}(\theta_2^{\alpha_2}) \otimes \tilde{R}(\theta_1^{\alpha_1}),$$

*ordered as mesh nodes, x-edge midpoints, y-edge midpoints, and cell centers. Furthermore, the Fourier representation of $\boldsymbol{R}$ is given by the $(1 \times 4)$-block-matrix*

$$\hat{\boldsymbol{R}}(\theta) = \left( \tilde{\boldsymbol{R}}(\theta^{(0,0)}) \ \tilde{\boldsymbol{R}}(\theta^{(1,0)}) \ \tilde{\boldsymbol{R}}(\theta^{(0,1)}) \ \tilde{\boldsymbol{R}}(\theta^{(1,1)}) \right).$$

The Fourier representation of $\boldsymbol{P}$ is given by a $(16 \times 4)$-matrix and

$$\hat{\boldsymbol{P}}(\theta) = \frac{1}{4} \left( \hat{\boldsymbol{R}}(\theta) \right)^H.$$

This approach can be extended to $Q_k$ or any other nodal basis for $Q_2$ as long as the 2D node points are given as a tensor-product of 1D meshes and the 2D basis functions are given as products of the 1D basis functions.

**Corollary 3.** *The restriction symbol for the $Q_k$ discretization in 2D can be written as a tensor product of the corresponding restriction symbol, $\tilde{R}^{(k)}(\theta^{\alpha})$, in 1D. That is, $\tilde{\boldsymbol{R}}^{(k)}(\boldsymbol{\theta}^{\alpha})$ is the $k^2 \times k^2$-matrix given by*

$$\tilde{\boldsymbol{R}}^{(k)}(\boldsymbol{\theta}^{\alpha}) = \tilde{R}^{(k)}(\theta_2^{\alpha_2}) \otimes \tilde{R}^{(k)}(\theta_1^{\alpha_1}),$$

*ordered correspondingly to the order of $\tilde{R}^{(k)}(\theta_1^{\alpha_1})$. Furthermore,*

$$\hat{\boldsymbol{P}}^{(k)}(\theta) = \frac{1}{4} \left( \hat{\boldsymbol{R}}^{(k)}(\theta) \right)^H.$$

## 5.3 | A lower bound on optimal convergence in 2D

Here, we also discuss the weighted Jacobi relaxation for the $Q_2$ approximation in 2D. For simplicity, we omit the subscript $h$ for operators and symbols unless it is necessary in the following. The symbol of the two-grid error propagation operator is

$$\hat{\mathcal{M}}^{\text{TGM}}(\omega, \theta) = \left( I - \hat{\boldsymbol{P}}(\theta) \hat{A}_{2h}(2\theta)^{-1} \hat{\boldsymbol{R}}(\theta) \hat{A}_2(\theta) \right) \hat{\boldsymbol{S}}_2(\omega, \theta),$$

where

$$\hat{A}_{2h}(2\theta) = \tilde{A}_{2h}(2\theta_2) \otimes \tilde{B}_{2h}(2\theta_1) + \tilde{B}_{2h}(2\theta_2) \otimes \tilde{A}_{2h}(2\theta_1),$$
$$\hat{A}_2(\theta) = \text{diag}\left\{\tilde{A}_2(\theta^{(0,0)}), \tilde{A}_2(\theta^{(1,0)}), \tilde{A}_2(\theta^{(0,1)}), \tilde{A}_2(\theta^{(1,1)})\right\},$$
$$\hat{S}_2(\omega, \theta) = \text{diag}\left\{\tilde{S}(\omega, \theta^{(0,0)}), \tilde{S}(\omega, \theta^{(1,0)}), \tilde{S}(\omega, \theta^{(0,1)}), \tilde{S}(\omega, \theta^{(1,1)})\right\},$$
$$\hat{R}(\theta) = \left(\tilde{R}(\theta^{(0,0)}), \tilde{R}(\theta^{(1,0)}), \tilde{R}(\theta^{(0,1)}), \tilde{R}(\theta^{(1,1)})\right),$$
$$\hat{P}(\theta) = \frac{1}{4}\left(\hat{R}(\theta)\right)^H,$$

in which

$$\tilde{S}(\omega, \theta^\alpha) = I - \omega \tilde{M}_2^{-1}(\theta)\tilde{A}_2(\theta^\alpha), \text{ with}$$

$$\tilde{M}_2(\theta) = \begin{pmatrix} \frac{112}{45} & 0 & 0 & 0 \\ 0 & \frac{176}{45} & 0 & 0 \\ 0 & 0 & \frac{176}{45} & 0 \\ 0 & 0 & 0 & \frac{256}{45} \end{pmatrix}.$$

First, we take a look at the eigenvalues of $\tilde{M}_2^{-1}(\theta)\tilde{A}_2(\theta)$. The left of Figure 11 shows the eigenvalue distribution of $\tilde{M}_2^{-1}(\theta)\tilde{A}_2(\theta)$ over $[-\frac{\pi}{2}, \frac{3\pi}{2}]^2$. Note that both the smallest and the biggest eigenvalues are achieved over the low frequencies, $[-\frac{\pi}{2}, \frac{\pi}{2}]^2$. As shown at the right of Figure 11 and discussed in more detail below, the standard smoothing analysis fails to predict the two-grid convergence factor in this case as well.

Motivated by the analysis in Section 3.3, we consider the limiting behavior of $\hat{\mathcal{M}}_h^{\text{TGM}}(\omega, \theta)$ when $\theta \to 0$. We first look at the range of the restriction operator when $\theta = (0, 0)$. From Corollary 2, we can calculate $\hat{R}(\mathbf{0})$, given by

$$\tilde{R}(0,0) = \begin{pmatrix} 1 & \frac{1}{2} & \frac{1}{2} & \frac{1}{4} \\ 1 & \frac{3}{2} & \frac{1}{2} & \frac{3}{4} \\ 1 & \frac{1}{2} & \frac{3}{2} & \frac{3}{4} \\ 1 & \frac{3}{2} & \frac{3}{2} & \frac{9}{4} \end{pmatrix}, \quad \tilde{R}(\pi, 0) = \begin{pmatrix} 1 & 0 & \frac{1}{2} & 0 \\ -1 & 0 & -\frac{1}{2} & 0 \\ 1 & 0 & \frac{3}{2} & 0 \\ -1 & 0 & -\frac{3}{2} & 0 \end{pmatrix},$$

$$\tilde{R}(0,\pi) = \begin{pmatrix} 1 & \frac{1}{2} & 0 & 0 \\ 1 & \frac{3}{2} & 0 & 0 \\ -1 & -\frac{1}{2} & 0 & 0 \\ -1 & -\frac{3}{2} & 0 & 0 \end{pmatrix}, \quad \tilde{R}(\pi, \pi) = \begin{pmatrix} 1 & 0 & 0 & 0 \\ -1 & 0 & 0 & 0 \\ -1 & 0 & 0 & 0 \\ 1 & 0 & 0 & 0 \end{pmatrix}.$$
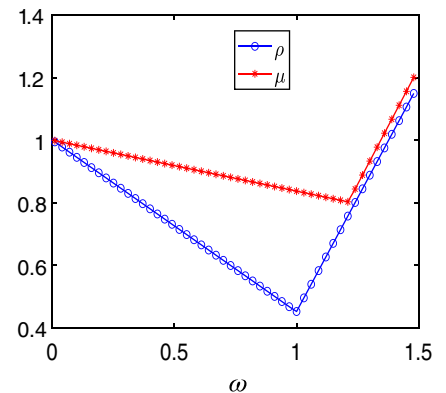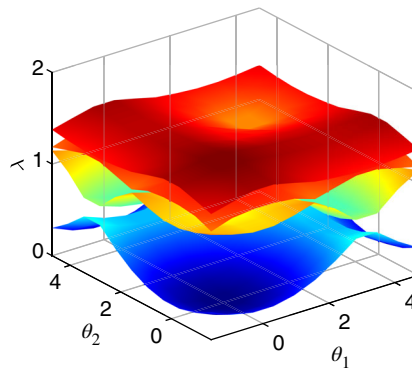


**FIGURE 11** At left, the distribution of eigenvalues, $\lambda$, of $\tilde{M}_2^{-1}(\theta)\tilde{A}_2(\theta)$ as a function of $\theta = (\theta_1, \theta_2)$. At right, local Fourier analysis-predicted two-grid convergence and smoothing factors as a function of $\omega$ for the $Q_2$ approximation in two dimensions

Note that the dimensions of the null spaces of $\tilde{R}(\pi, 0)$, $\tilde{R}(0, \pi)$ and $\tilde{R}(\pi, \pi)$ are 2, 2, and 3, respectively. Because $\hat{P}(0) = \frac{1}{4}\hat{R}(0)^H$, we can easily identify seven vectors that are not treated by CGC, and provide a lower bound on the two-grid convergence behavior.

To find the seven vectors (and the associated eigenvalues of $\lim_{\theta \to 0} \hat{\mathcal{M}}^{\text{TGM}}(\omega, \theta)$), we consider the high frequencies corresponding to $(\theta_1^0, \theta_2^0) = (0, 0)$. Let $T_2 = \tilde{M}_2^{-1}(\theta)\tilde{A}_2(\pi, 0)$, $T_3 = \tilde{M}_2^{-1}(\theta)\tilde{A}_2(0, \pi)$, and $T_4 = \tilde{M}_2^{-1}(\theta)\tilde{A}_2(\pi, \pi)$. By standard calculation, we have

$$
T_2 = \begin{pmatrix} \frac{29}{28} & 0 & -\frac{1}{2} & 0 \\ 0 & 1 & 0 & -\frac{6}{11} \\ -\frac{7}{22} & 0 & 1 & 0 \\ 0 & -\frac{3}{8} & 0 & 1 \end{pmatrix}, \quad
T_3 = \begin{pmatrix} \frac{29}{28} & -\frac{1}{2} & 0 & 0 \\ -\frac{7}{22} & 1 & 0 & 0 \\ 0 & 0 & 1 & -\frac{6}{11} \\ 0 & 0 & -\frac{3}{8} & 1 \end{pmatrix}, \quad
T_4 = \begin{pmatrix} \frac{15}{14} & 0 & 0 & 0 \\ 0 & 1 & 0 & 0 \\ 0 & 0 & 1 & 0 \\ 0 & 0 & 0 & 1 \end{pmatrix}.
$$

Standard calculation shows that $T_2$ has two eigenvalues, $\hat{\lambda}_{1,2} = 1 \pm \sqrt{\frac{9}{44}}$, with the corresponding eigenvectors $x_{1,2} = \left(0 \ 1 \ 0 \ \pm\sqrt{\frac{11}{16}}\right)$, which are in the null space of $\tilde{R}(\pi, 0)^H$. Denote $\hat{x}_{1,2} = \left(z \ x_{1,2} \ z \ z\right)^T$, where z stands for a zero vector with size $1 \times 4$. Similarly, it is easy to check that $\hat{\lambda}_{3,4} = 1 \pm \sqrt{\frac{9}{44}}$ are the two eigenvalues of $T_3$ corresponding to eigenvectors $x_{3,4} = \left(0 \ 0 \ 1 \ \pm\sqrt{\frac{11}{16}}\right)$. Denote $\hat{x}_{3,4} = \left(z \ z \ x_{3,4} \ z\right)^T$.

Finally, the structure of $T_4$ tells us that it has three eigenvalues: $\hat{\lambda}_{5,6,7} = 1$ and the corresponding eigenvectors are $x_5 = \left(0 \ 1 \ 0 \ 0\right)$, $x_6 = \left(0 \ 0 \ 1 \ 0\right)$, $x_7 = \left(0 \ 0 \ 0 \ 1\right)$, which are in the null space of $\tilde{R}(\pi, \pi)^H$. Denote $\hat{x}_5 = \left(z \ z \ z \ x_5\right)^T$, $\hat{x}_6 = \left(z \ z \ z \ x_6\right)^T$, $\hat{x}_7 = \left(z \ z \ z \ x_7\right)^T$.

The above discussion gives seven eigenvalues of the two-grid operator $\lim_{\theta \to 0} \hat{\mathcal{M}}^{\text{TGM}}(\omega, \theta)$, leading to the following results.

**Lemma 2.**

$$
\min_\omega \left\{ \max \{|\lambda^{**}|\} : \lambda^{**} = 1 - \omega\hat{\lambda}_j, 1 \le j \le 7 \right\} = \sqrt{\frac{9}{44}} \approx 0.4523, \tag{36}
$$

*and only $\omega = \omega_2^* = 1$ achieves the minimum.*

*Proof.* Since the smallest and largest values of $\hat{\lambda}_j (j = 1, 2, \cdots, 7)$ are $1 - \sqrt{\frac{9}{44}}$ and $1 + \sqrt{\frac{9}{44}}$, respectively, the optimal $\omega$ for (36) is $\omega_2^* = \frac{2}{1 + \sqrt{\frac{9}{44}} + 1 - \sqrt{\frac{9}{44}}} = 1$. It follows $1 - \omega_2^* \left(1 - \sqrt{\frac{9}{44}}\right) = \sqrt{\frac{9}{44}}$. ∎
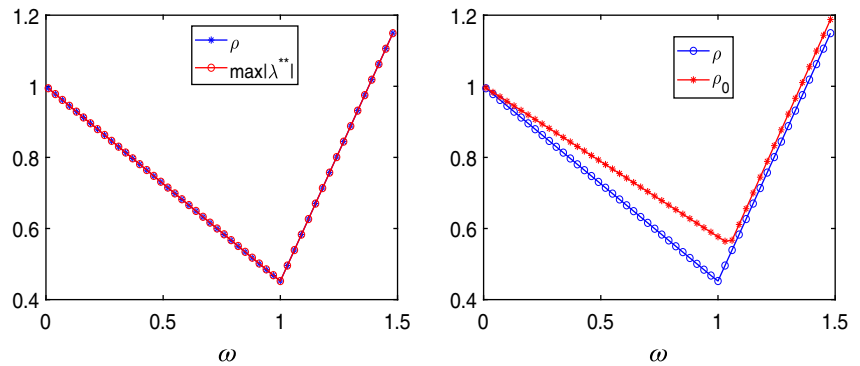
**Corollary 4.** *For any $\omega$, the optimal convergence factor for the two-grid algorithm using a single weighted Jacobi relaxation on the $Q_2$ discretization in 2D, is not less than $\sqrt{\frac{9}{44}}$, and this factor can be achieved if and only if $\omega = \omega_2^*$.*

In order to see how the parameter $\omega_2^*$ performs in practice in a multigrid method, we present two- and multigrid results. First, we use the optimal parameter, $\omega = 1.2$, corresponding to the smoothing factor (obtained by numerical optimization) to show the multigrid performance (Table 5). Table 5 also shows that $\omega_2^*$ achieves the best possible results, with measured two-grid convergence factors that coincide with the LFA-predicted convergence factors. The same convergence factor is also obtained using full $V$ cycles. Comparing these results suggests that choosing the right parameter for efficient multigrid is very important for the higher-order approximation and traditionally optimizing the smoothing factor is not

|  | $\omega = 1.2, \mu = 0.815$ | | | | $\omega = \omega_2^* = 1.000, \mu = 0.842$ | | | |
|---|---|---|---|---|---|---|---|---|
|  | TG(1) | TG(2) | TG(3) | TG(4) | TG(1) | TG(2) | TG(3) | TG(4) |
| $\rho$ | 0.743 | 0.606 | 0.506 | 0.439 | 0.452 | 0.288 | 0.123 | 0.091 |
| $\hat{\rho}_{h=1/256}$ | 0.742 | 0.606 | 0.505 | 0.438 | 0.452** | 0.288 | 0.123 | 0.091 |
|  | V(1) | V(2) | V(3) | V(4) | V(1) | V(2) | V(3) | V(4) |
| $\hat{\rho}_{h=1/256}$ | 0.742 | 0.686 | 0.463 | 0.487 | 0.452** | 0.288 | 0.118 | 0.092 |

**TABLE 5** Multigrid convergence factors for the $Q_2$ approximation in two dimensions. Note that for the case of $\hat{\rho}_{h=1/256}$ and $\omega = 1$, an alternating convergence pattern was used, so the reported convergence factor is averaged over the final two iterations before convergence (denoted **).

**FIGURE 12** At left, local Fourier analysis (LFA)-predicted two-grid convergence factor and max$\{|\lambda^{**}|\}$ as a function of $\omega$. At right, LFA-predicted two-grid convergence factor and $\rho_0$, for the $Q_2$ approximation in two dimensions



suitable for optimizing the two-grid convergence factor. In Table 5, we also note some small discrepancies between the predicted and measured two-grid convergence factors and those achieved by full $V$ cycles. While these do not appear to be significant (particularly since the most cost-effective cycles use only 1 relaxation sweep per iteration and no degradation is seen here), this may be a case where three-grid analysis can provide some insight.[5]

## 5.4 | A modified two-grid analysis for the $Q_2$ approximation in 2D

Considering the classical LFA smoothing and convergence factors, the right of Figure 11 indicates that the optimal $\omega$ minimizing the two-grid convergence factor is 1, and that the LFA smoothing factor fails to predict the two-grid convergence factor for the $Q_2$ finite-element approximation in 2D.

In contrast, we plot the LFA-predicted two-grid convergence factor and max$\{|\lambda^{**}|\}$ as defined in Equation (36) as a function of $\omega$, at the left of Figure 12. This shows that for all $\omega$, the two-grid convergence factor is given by max$\{|\lambda^{**}|\}$, and that convergence is dominated by the harmonic space associated with $\boldsymbol{\theta} = (0, 0)$.

The modified prediction given by defining $Q_0$ using the limit in Equation (25) and $\rho_0$ as in Equation (26) can also be extended to this case. We plot $\rho_0$, compared with the true convergence factor at the right of Figure 12. We see that $\rho_0$ again overpredicts the convergence factor, as $Q_0$ captures poorly the true effects of CGC for values of $(\theta_1, \theta_2)$ near $(\pm\frac{\pi}{2}, \pm\frac{\pi}{2})$. However, $\rho_0$ still offers a reasonable prediction of convergence and of the optimal relaxation parameter.

*Remark* 9. The modified two-grid analysis presented here can be extended to the 3D Laplacian and more general classes of PDEs, such as anisotropic problems, linear elasticity and Stokes, as well as to $P_k$ finite-element discretizations. However, we note that, as always, challenges are expected for high dimensional or complicated systems and that the corresponding modified two-grid symbols will have large dimensions. For example, with $Q_2$ elements for the 3D Laplacian, the two-grid symbol will be of size $64 \times 64$, coupling 8 types of DoF with 8 harmonic frequencies. At such scales, theoretical analysis seems impossible, but LFA may still offer some insights.

## 6 | CONCLUSION

In this paper, we apply classical LFA to analyze and optimize the two-grid convergence factor for multigrid methods with higher-order finite-element approximations, especially focusing on optimal parameter choice for quadratic Lagrange elements in 1D and 2D. However, we find that minimizing the classical LFA smoothing factor fails to accurately predict the two-grid convergence factor. To overcome this limitation, we develop an alternate idealized CGC operator that, in combination with relaxation analysis, offers a reliable prediction of multigrid performance that is simpler to compute than the standard two-grid LFA convergence factor. Determining optimal parameters that minimize the resulting convergence factor is then possible. With the parameters chosen based on the modified LFA, we see good agreement between the measured convergence factor and predicted LFA convergence factor with periodic boundary conditions. Compared with the traditional parameter choice based on minimizing the classical smoothing factor, we note a big improvement in performance with the corrected parameters. This may also explain why the LFA smoothing factor cannot predict the two-grid convergence factor for higher-order finite-element approximations for other types of PDEs, such as the $Q_2$-$Q_1$ approximation to the Stokes equations, which was observed in the work of MacLachlan and Oosterlee[9] Our exploration here for Jacobi relaxation is a first step to better understand how to use LFA properly. It will be interesting to look at

other relaxation schemes, such as multicolor relaxation for these higher-order approximations, where the unknowns are located on staggered meshes, to design efficient algorithms. Moreover, considering different bases choices for the same finite-element space is another possible direction for future work, to determine whether there is a basis choice such that the standard smoothing analysis can offer a sharp prediction of actual performance.

## CONFLICT OF INTEREST
This work does not have any conflicts of interest.

## ORCID
*Yunhui He* https://orcid.org/0000-0003-3476-2487
*Scott MacLachlan* https://orcid.org/0000-0002-6364-0684

## REFERENCES
1. Briggs WL, Henson VE, McCormick SF. A multigrid tutorial. Philadelphia, PA: SIAM, 2000.
2. Hackbusch W. Multi-Grid methods and applications. Vol 4. Springer, Berlin: Springer Science & Business Media, 2013.
3. Stüben K, Trottenberg U. Multigrid methods: Fundamental algorithms, model problem analysis and applications. Multigrid methods. Berlin, Heidelberg: Springer, 1982; p. 1–176.
4. Wesseling P. An introduction to multigrid methods. Pure and applied mathematics. Chichester, NH: John Wiley & Sons, Ltd., 1992.
5. Wienands R, Joppich W. Practical Fourier analysis for multigrid methods. Boca Raton, FL: Chapman and Hall/CRC press, 2005.
6. Heys J, Manteuffel T, McCormick S, Olson L. Algebraic multigrid for higher-order finite elements. J Comput Phys. 2005;204(2):520–532.
7. Trottenberg U, Oosterlee CW, Schüller A. Multigrid. San Diego, CA: Academic Press, Inc., 2001.
8. Boonen T, Van Lent J, Vandewalle S. Local Fourier analysis of multigrid for the curl-curl equation. SIAM J Sci Comput. 2008;30(4):1730–1755.
9. MacLachlan SP, Oosterlee CW. Local Fourier analysis for multigrid with overlapping smoothers applied to systems of PDEs. Numer Linear Algebra Appl. 2011;18(4):751–774.
10. Friedhoff S, MacLachlan S, Börgers C. Local Fourier analysis of space-time relaxation and multigrid schemes. SIAM J Sci Comput. 2013;35(5):S250–S276.
11. Vandewalle S, Horton G. Fourier mode analysis of the multigrid waveform relaxation and time-parallel multigrid methods. Computing. 1995;54(4):317–330.
12. Drzisga D, John L, Rüde U, Wohlmuth B, Zulehner W. On the analysis of block smoothers for saddle point problems. SIAM J Matrix Anal Appl. 2018;39(2):932–960.
13. Gaspar FJ, Notay Y, Oosterlee CW, Rodrigo C. A simple and efficient segregated smoother for the discrete Stokes equations. SIAM J Sci Comput. 2014;36(3):A1187–A1206.
14. Luo P, Rodrigo C, Gaspar FJ, Oosterlee CW. On an Uzawa smoother in multigrid for poroelasticity equations. Numer Linear Algebra Appl. 2017;24(1):E2074.
15. Hemker PW, Hoffmann W, Van Raalte M. Fourier two-level analysis for discontinuous Galerkin discretization with linear elements. Numer Linear Algebra Appl. 2004;11(5-6):473–491.
16. Rodrigo C, Salinas P, Gaspar FJ, Lisbona FJ. Local Fourier analysis for cell-centered multigrid methods on triangular grids. J Comput Appl Math. 2014;259:35–47.
17. Friedhoff S, MacLachlan S. A generalized predictive analysis tool for multigrid methods. Numer Linear Algebra Appl. 2015;22(4):618–647.
18. Donatelli M, Garoni C, Manni C, Serra-Capizzano S, Speleers H. Symbol-based multigrid methods for Galerkin B-spline isogeometric analysis. SIAM J Numer Anal. 2017;55(1):31–62.
19. de la Riva ÁP, Rodrigo C, Gaspar FJ. An efficient multigrid solver for isogeometric analysis. June 2018. arXiv:1806.05848.
20. Rodrigo C, Gaspar FJ, Lisbona FJ. Multicolor Fourier analysis of the multigrid method for quadratic FEM discretizations. Appl Math Comput. 2012;218(22):11182–11195.
21. May DA, Brown J, Le Pourhiet L. A scalable, matrix-free multigrid preconditioner for finite element discretizations of heterogeneous Stokes flow. Comput Methods Appl Mech Eng. 2015;290:496–523.
22. Maday Y, Muñoz R. Spectral element multigrid. II. theoretical justification. J Sci Comput. 1988;3(4):323–353.
23. Rønquist EM, Patera AT. Spectral element multigrid. I. formulation and numerical results. J Sci Comput. 1987;2(4):389–406.
24. Köster M, Turek S. The influence of higher order FEM discretisations on multigrid convergence. Comput Methods Appl Math. 2006;6(2):221–232.
25. Sundar H, Stadler G, Biros G. Comparison of multigrid algorithms for high-order continuous finite element discretizations. Numer Linear Algebra Appl. 2015;22(4):664–680.
26. Brown J. Efficient nonlinear solvers for nodal high-order finite elements in 3D. J Sci Comput. 2010;45(1-3):48–63.

27. John V, Matthies G. Higher-order finite element discretizations in a benchmark problem for incompressible flows. Int J Numer Methods Fluids. 2001;37(8):885–903.

28. John V. Higher order finite element methods and multigrid solvers in a benchmark problem for the 3D Navier-stokes equations. Int J Numer Methods Fluids. 2002;40(6):775–798.

29. Rodrigo C, Sanz F, Gaspar FJ, Lisbona FJ. Local Fourier analysis for edge-based discretizations on triangular grids. Numerical Math: Theory Methods Appl. 2015;8(1):78–96.

30. Brown J, He Y, MacLachlan SP. Local Fourier analysis of BDDC-like algorithms. SIAM J Sci Comput. 2019;41(5):S346–S369.

31. Hemker PW, Hoffmann W, van Raalte MH. Two-level Fourier analysis of a multigrid approach for discontinuous Galerkin discretization. SIAM J Sci Comput. 2003;25(3):1018–1041.

32. Rathgeber F, Ham DA, Mitchell L, et al. Firedrake: Automating the finite element method by composing abstractions. ACM Trans Math Softw. 2016;43(3):24:1–24:27.

33. Kirby R, Mitchell L. Solver composition across the PDE/linear algebra barrier. SIAM J Sci Comput. 2018;40(1):C76–C98.

34. Balay S, Abhyankar S, Adams MF, et al. PETSc web page. 2019. Available from: http://www.mcs.anl.gov/petsc.

35. Balay S, Abhyankar S, Adams MF, et al. PETSc users manual. ANL-95/11 - Revision 3.11. Argonne National Laboratory. 2019. Available from: http://www.mcs.anl.gov/petsc.

36. Niestegge A, Witsch K. Analysis of a multigrid Stokes solver. Appl Math Comput. 1990;35(3):291–303.